12-2021

Materials and process design for ceramic fused filament fabrication (CF3) of hydroxyapatite.

Kavish Sudan
University of Louisville

Recommended Citation

Sudan, Kavish, "Materials and process design for ceramic fused filament fabrication (CF3) of hydroxyapatite." (2021). *Electronic Theses and Dissertations.* Paper 3795.
https://doi.org/10.18297/etd/3795

MATERIALS AND PROCESS DESIGN FOR CERAMIC FUSED FILAMENT FABRICATION (CF^3) OF HYDROXYAPATITE

By
Kavish Sudan
B.E Mechanical, University of Jammu, 2017

A Thesis
Submitted to the faculty of the
J. B. Speed School of Engineering of University of Louisville
In Partial Fulfillment of the Requirements
for the Degree of

Master of Science
in Mechanical Engineering

Department of Mechanical Engineering
University of Louisville
Louisville, Kentucky

December 2021

MATERIALS AND PROCESS DESIGN FOR CERAMIC FUSED FILAMENT FABRICATION (CF^3) OF HYDROXYAPATITE

By

Kavish Sudan
B.E Mechanical, University of Jammu, 2017

A Thesis Approved on

December 1, 2021

by the following Thesis Committee:

Dr. Kunal Kate

Dr. Sundar Atre

Dr. Jagannadh Satyavolu

ACKNOWLEDGEMENTS

This thesis is dedicated to my parents

Mr. Novat Ram

and

Mrs. Sushil Kumari

And the loving memory of my grandmother.

I would like to express my deep sense of gratitude and profound respect towards my advisor Dr. Kunal Kate of J.B. Speed School of Engineering at University of Louisville, who has helped and encouraged me at all stages of my thesis work with great patience and immense care. Throughout the course of my research journey, he has steered me in the right direction and given me great support throughout the work process. Without his guidance and persistent help, this thesis would not have been possible.

I am particularly indebted to Dr. Vamsi K. Balla, who despite being extraordinarily busy with his duties, took time to hear, guide and keep me on the correct path. His wholehearted participation in discussions and his insightful suggestions helped shape this research project.

I would also like to thank Dr. Sundar Atre for giving me the opportunity to join his research group, Materials Innovation Guild. Throughout my research journey, he always encouraged me to express my ideas. He guided me through tough times and was with me to check on my research progress. His sincere dedication to his students is both admirable and inspirational. It was a privilege to work with him and learn from him.

These acknowledgements would not be complete without mentioning my lab colleagues Param, Qasim, Arul, Dr. Subrata Debnath and Dr. Azim Gökçe. It was a great pleasure working among such talented individuals and I deeply appreciate their ideas, help and good humor.

A special thanks to Dr. Gautam Gupta whose door is always open and who was always willing to offer advice, suggestions for improving my thesis or just lively conversation.

Lastly, I would like to thank my family, especially Mom and Dad, for the continuous support they have given me throughout my time in graduate school; I could not have done it without them.

This work would not have been possible without the financial support from NSF-EPSCoR–RII Track-1: Kentucky Advanced Manufacturing Partnership for Enhanced Robotics and Structures (Award #1849213) and NASA.

ABSTRACT

MATERIALS AND PROCESS DESIGN FOR CERAMIC FUSED FILAMENT FABRICATION (CF^3) OF HYDROXYAPATITE

Kavish Sudan

December 1,2021

Ceramic fused filament fabrication (CF3) enables the fabrication of highly customizable ceramic parts at relatively lower costs compared to other AM technologies. Advanced ceramics, having specific or niche applications, call for a high level of accuracy to meet the performance requirements. For achieving the desired level of accuracy in any manufacturing process, it is important to know the effect of involved parameters at different stages of fabrication. CF3 has been around for a while but there has been a severe lack of literature dealing with understanding the effect of process parameters on the final part properties. In this study, Hydroxyapatite (HAp) components with 75 wt.% solids loading filaments were prepared. A DOE was conducted to analyze and establish the relationship between process parameters and the final printed part properties. Extrusion multiplier, % infill, and print speed were taken as input parameters and the effect of their effect on final part dimensions, layer thickness, bead width, and surface roughness were analyzed. Additionally, the experimental data was analyzed using regression analysis, analysis of variance (ANOVA), % contribution, and main effects using Minitab software.

Furthermore, to establish the capability of HAp CF3 in biomedical applications, HAp and its composite parts with 10 wt.% Si3N4 (HAp10SN) were fabricated.

Homogeneous feedstock with 63 wt.% ceramic powder was prepared and used to extrude filaments for further printing using a desktop printer. Our results showed that the addition of Si3N4 to HAp increases the feedstock viscosity. However, the filaments and CF3 parts made using HAp and HAp10SN feedstocks exhibited comparable densities without gross defects. We have obtained relatively smoother CF3 parts with HAp10SN than pure HAp, which is attributed to their high feedstock viscosity and formation of the liquid phase during sintering. Sintering at 1250 °C for 4 h in air, after thermal debinding, resulted in a relative density of ~85% with HAp and tricalcium phosphate (TCP) as major constituents. Sintered HAp10SN samples also revealed an almost 70% reduction in the grain size and 147% increase in the hardness compared to pure HAp. Our results indicate that the CF3 processed HAp10SN samples containing ~15% porosity, Si3N4 particles, and Si-substituted HAp/TCP have strong potential as bone replacements.

TABLE OF CONTENTS

PAGE

PAGE

PAGE

LIST OF TABLES

LIST OF FIGURES

CHAPTER 1

INTRODUCTION

Ceramics, as a class, usually represent hard, brittle, thermally and electrically insulative, refractory, and chemically inert inorganic materials. Owing to these inherent properties, these have traditionally been used for applications ranging from sanitary ware and decorative pottery to ceramic engines and cutting tools. Moreover, there exist special sub-classes of ceramics that exhibit electrical conductivity and bioactivity, which further expand the scope and applications of ceramic materials.

Traditionally, ceramics processing utilizes already established manufacturing processes such as powder pressing, and injection molding followed by sintering and machining. These manufacturing processes are highly efficient in the case of larger lot sizes and simple geometries but lack affordability when it comes to the fabrication of customized parts and prototypes, owing largely to high tooling costs. This gets crucial in the case of advanced ceramics and bioceramics as their application area may call for fine structures, complex geometries, and/or controlled pores size and interconnectivity. An approach to fabricate customizable parts without using specialized tooling is using additive manufacturing (AM). This involves forming a component layer by layer based on a 3D model. Depending on the raw material used and method of layer formation, the AM technologies currently capable of fabricating ceramic components can be grouped as slurry-based (stereolithography, inkjet printing, direct ink writing, digital light processing), powder-bed based (selective laser sintering/melting, binder jetting) and material extrusion-based (fused filament fabrication, robocasting). Among these, fused filament fabrication is currently the most popular AM technology having around 41% of the total market share. This can be attributed largely to the relatively inexpensive equipment and ease of operation involved in the process. At its core, fused filament fabrication (FFF) is an extrusion-based additive manufacturing process in which a polymer-based filament (mostly thermoplastic) is passed through a nozzle fitted into a heated liquefier and then deposited on a platform in a semi-solid state, layer by layer until the desired geometry is achieved. The same process can be utilized to fabricate ceramic parts by using composite filament with a thermoplastic polymer as the matrix and ceramic powder as filler element. The composite parts printed using the filaments are then debound to remove polymeric components and then sintered to obtain dense ceramic parts. This modified process, termed ceramic fused filament fabrication, works similar to polymer FFF, but the added steps and multi-modal nature of the raw material called for a structured research study to better understand the process-parameter relationship.

In CHAPTER 2 a HAp powder-polymer feedstock was prepared with 75 wt.% solids loading and subsequently extruded into filaments with 1.75 mm diameter and 3D printed into cuboids with 10 x 10 x 15 mm dimensions using the CF3 process. To identify the influence of CF3 3D printing process parameters on effectively fabricating HAp parts, an L9 Taguchi design of experiments (DOE) based study was performed. The CF3 printing parameters such as infill %, printing speed, and extrusion multiplier were varied at three levels in these experiments. CF3 parts were characterized for dimensions, surface roughness parallel (∥) and perpendicular (⊥) to the 3D printing direction, bead width, layer thickness, part fill%, and relative density of part walls. Additionally, the experimental data was analyzed using regression analysis, analysis of variance (ANOVA), % contribution, and main effects of each process parameter to identify key process parameters that influence in obtaining parts with desired dimensions and tolerance using CF3 printing. It is expected that the current study will provide insights for effectively printing parts that are important for patient-specific 3D printing and designing experiments for the CF3 process when printing with high solids loading 63 wt.% HAp powder-polymer filaments.

CHAPTER 3 discusses debinding and sintering of printed HAp parts and establishing the capability of CF3 to fabricate customizable dense HAp structures for application in biomedical implants. In this investigation, hydroxyapatite (HAp) and its composite parts with 10 wt.% Si3N4 (HAp10SN) using CF3 Feedstocks with 75 wt.% ceramic powder were prepared followed by filament extrusion for printing. It was found that the addition of Si3N4 increases the viscosity of the feedstock, but the filaments and CF3 parts made using both feedstocks exhibited comparable densities without any printing-induced gross defects. A three-step thermal debinding cycle developed using thermogravimetric analysis of the feedstock resulted in complete removal of the binder and a sintered density of ~85% was achieved in both samples. Sintered HAp10SN samples were relatively smoother than pure HAp samples due to their high feedstock viscosity which reduced material overflow during printing. Almost 70% reduction in the grain size was observed with the addition of Si3N4 to HAp due to the formation of liquid phase during sintering, which increased the hardness. Our results indicate that present CF3 processed HAp10SN samples containing ~ 15% total porosity with Si3N4 particles and potential Si-substituted HAp/TCP could show potentially superior biological performance than pure HAp. However, further studies are required to achieve microstructural uniformity and confirm the anticipated biological performance of these CF3 processed HAp10SN ceramics for bone replacement applications.

CHAPTER 2

DESIGN OF EXPERIMENTS FOR CERAMIC FUSED FILAMENT FABRICATION (CF^3) 3D PRINTING WITH HYDROXYAPATITE POWDER POLYMER FILAMENTS

2.1 Introduction

Hydroxyapatite (HAp, Ca10(PO4)6(OH)2) had been utilized in a variety of bone implant applications due to its excellent bioactivity, osteoconductivity, and its similarity to the natural bone in terms of material properties [1-4]. Most widely utilized HAp specimens include discs and rods that are made using a press and sinter manufacturing process [1-4]. These limited geometries achievable using conventional manufacturing processes restrict the scope of its applications despite the excellent biological properties of HAp. Other manufacturing processes such as ceramic injection molding (CIM) can manufacture complex geometries out of ceramics, however, such processes are more suitable for mass production with a need to invest in molding tools. Additionally, in order to offset tooling costs, a minimum of 10,000-100,000 parts are needed [5-7]. This limits the use of CIM for making patient-specific implants fabricated on-demand to custom shape and size.

Additive manufacturing (AM) allows for the fabrication of 3D structures that are custom in shape and can cost-effectively produce parts for a limited batch size of 10-100 [5]. The Production lead times for additively manufactured parts are also faster compared to traditional manufacturing processes. In recent years, AM processes have successfully been utilized for fabricating a variety of medical implants made from ceramics [1, 8-10]. Current AM technologies that can process ceramics include binder jetting, laser powder bed fusion (LPBF), and ceramic fused filament fabrication (CF3). Both binders jetting and the LBPF AM process use a powder bed spread on a built platform to build a part layer-by-layer. In these processes, the powder particles are bonded together using either a liquid polymer binder or laser energy to melt the powder and consequently form a 3D shape. Challenges involve limited availability of proper powders (size, shape, type, and flow properties) and binders that can be suitably processed with these AM processes [9-11].

Alternatively, the CF3 process is highly open source and uses benchtop fused filament fabrication (FFF) 3D printers that are customizable according to the material being used. The CF3 process is a hybrid FFF process that uses a ceramic-powder polymer filament for forming the desired geometry and subsequently, the part undergoes binder removal by debinding and densification by sintering at elevated temperatures. Prior works which successfully demonstrate similar work to CF3 include 3D printing of metals, ceramics and other composites using a powder-filled polymer filament [8, 9, 12, 13]. Similar work performed by our group indicated a need for high solids loading in the powder-polymer system for better shape retention during the debinding and sintering [13, 14].

The most prominent work on HAp-polymer 3D printing performed by FFF process had a solids loading of 50 wt.% which as identified by our prior work in a CF3 process can cause issues of shape retention and polymer removal defects [12-14]. Additionally, while 3D printing with high solids loaded (>70 wt.%) powder-polymer filaments, it is important to identify appropriate process parameters that influence printing parts to desired specifications. Several prior works have looked at exploring FFF process parameters by performing a design of experiment analysis to identify key process parameters that affect part quality and properties [15-19].

However, there has been limited work done on identifying CF3 printing parameters that influence dimensional accuracy when printing with high solids loading powder-polymer filaments. Our previous work strongly indicated that material properties such as thermal conductivity, coefficient of thermal expansion, specific heat, and viscosity play an important role in affecting how part dimensions get affected and lead to warpages and internal stresses [13, 14]. Thus, the behavior of how a material flow, expands, deposits, and solidifies for filled and unfilled polymers filaments is dictated by its thermomechanical properties. Additionally, the material type and its properties dictate the quality of printed parts at different print speeds and nozzle temperatures [13, 14].

The success of post-printing processes such as debinding and densification involved in CF3 process strongly depends on the green density and overall quality of printed parts as for any pores/ defects and geometrical deviations in these green parts are detrimental to the sintered part properties and quality. Therefore, in addition to high-density feedstock filaments, an appropriate combination of printing parameters is also one of the prerequisites to produce high-quality and high-strength sintered parts. Therefore, the current work addresses gap in identifying how to print speed and extrusion multiplier affect print quality, and further to ascertain their influence in shape and feature resolution a variation in infill % is performed. L9 Taguchi design of experiments and analysis was performed on HAp powder-polymer 3D printed parts. A high solids loading, 63 wt.% HAp powder-polymer feedstock was prepared which was extruded into a filament. Subsequently, the HAp filament was used for 3D printing cuboids specimens. The HAp printed parts were characterized for surface roughness, dimensions, volume fraction filled, bead width, and layer thickness. Analysis of variance (ANOVA), regression analysis, and main effects plot was plotted to identify the influence of each 3D printing process parameter. It is expected that the current work will allow for use of the CF3 process to fabricate parts with the desired shape and quality and identify factors that influence the processing of high solids loaded ceramic powder-polymer filaments that can enable fabricating complex patient-specific 3D geometries when printing with HAp filaments.

2.2 Materials and Methods:

2.2.1 Materials and Processing:

Commercially available hydroxyapatite (HAp) powder with an average particle size of 20 µm was used as starting material to prepare HAp-polymer binder feedstock. A scanning electron microscope (SEM, TESCAN USA, Inc., Warrendale, PA, USA) was used to image the HAp powders for their morphology. A HAp - multi-component polymer binder feedstock with 63 wt.% was compounded in an Intelli-Torque Brabender Mixer. The HAp feedstock was mixed at 180°C and 50 rpm for 45 min to achieve uniform mixing of HAp powders within the polymer binder and a batch size of 300 g was prepared. The feedstock was then extruded into filaments of 1.75 ± 0.05 mm diameter using a capillary die with an L/D ratio of 30/1.75mm on a Goettfert Rheograph 20. The extrusion temperature was 105 °C with a uniform extrusion speed of 0.1 mm/s. The filaments were subsequently used for Ceramic Fused Filament Fabrication (CF^3) 3D printing.

A proprietary polymer binder was used for the compounding of feedstock, and filament for 3D printing. For manufacturing purposes, the feedstock composition is represented by weight and the conversion of volume fraction for powder and binder from mass fraction was calculated using **Equation 1.**

$$\phi_p = \frac{\frac{X_p}{\rho_p}}{\frac{X_p}{\rho_p} + \frac{X_b}{\rho_b}} \quad \phi_b = \frac{\frac{X_b}{\rho_b}}{\frac{X_p}{\rho_p} + \frac{X_b}{\rho_b}}$$

Equation 1

where, ρ is the density, X is the mass fraction, ϕ is the volume fraction and the subscripts c, b and p stand for the composite, binder, and powder respectively.

The HAp powder, polymer binder, and HAp feedstock were characterized for their true density using a Micromeritics Accupyc II 1340 helium gas pycnometer. This information was used to convert mass fraction to volume fraction in **Equation 1**.

2.2.2 Design of experiments for CF^3 3D printing of HAp filaments

The 63 wt.% HAp filaments were used to optimize the CF^3 3D printing process using a Makergear-M2 3D printer. To understand the sensitivity of CF^3 3D printing parameters to achieve desired dimensional accuracy, printed volume, and surface roughness, three critical process parameters, namely infill %, print speed and extrusion multiplier were varied. The three levels of these parameters developed using an L_9 Taguchi design of experiments are shown in **Table 1.** Other CF^3 printing parameters that were kept constant include, layer thickness of 200µm, bead width of 600 µm, print temperature of 245°C, and bed temperature of 75°C. A cuboid geometry with length × width × height of 10 × 10 × 15 mm was designed in Solidworks, shown in **Figure 1a,** for performing 3D printing experiments. This specific geometry was selected as it allows us to understand the printability of the present 63 wt.% HAp filaments in terms of shape retention of parts with aspect ratio more than 1. Additionally, the shape also provides ease of dimensional and volume measurements of the printed parts.

Table 1. L-9 Taguchi design of experiments for 3D printing

DOE, #	**Infill, %**	**Print speed, mm/s**	**Extrusion multiplier, a.u.**
1	75	10	0.8
2	75	15	1
3	75	20	1.2
4	50	10	1
5	50	15	1.2
6	50	20	0.8
7	25	10	1.2
8	25	15	0.8
9	25	20	1

The Solidworks part file was saved in .stl format and was imported into a 3D printing process software (Simplify3D) to create g-code following by printing with process conditions mentioned in **Table 1**. **Figure 1b** shows representative images of sliced geometries with various infill %. Four parts were printed for each DOE process condition listed in **Table 1** and for 100% infill printed part, which was used as a control sample.

2.2.3 Material Characterization and Analysis of CF^3 Printed HAp Parts

The dimensions of the 3D printed parts were measured using calipers to calculate the volume for the parts. Additionally, comparisons of measured dimensions and volume were also made with CAD part volume to understand the limits of 3D printed part tolerances. Four measurements were performed on each dimension of the 3D printed parts. Additionally, the surface roughness of the 3D-printed parts was measured in the parallel (‖) and perpendicular (⊥) to the 3D printing direction using a portable surface roughness tester (Surftest SJ-210, Mitutoyo America Corporation, Mason, OH, USA). These measurements were conducted using a scan length of 5 mm at 0.5 mm/s speed. Optical microscopy and images analysis was conducted using an Olympus BX-51 microscope to measure layer thickness and bead width of the 3D printed geometries. To calculate the actual printed infill volume occupied for the designed part geometry experimentally, which is referred to as infill%, actual open porosity in the parts was calculated using **Equation 2.** The infill % calculations accounted for designed voids in the parts due to infill% variations as shown in **Table 1** by measuring closed porosity in the printed part by Archimedes density measurements of the part walls and total porosity measurements by calculating total part density by mass by volume relationships as shown in **Equation 3 – Equation 6**. The density of HAp feedstock was estimated at 1.65 g/cm^3 and was taken as a basis from our prior work [20].

$$Infill\,\% = 100 - Actual\ open\ porosity \qquad \textbf{Equation 2}$$

$$Actual\ open\ porosity = Total\ porosity - Closed\ porosity \qquad \textbf{Equation 3}$$

$$Closed\ porosity = 100 - Relative\ density\ of\ the\ part\ walls \qquad \textbf{Equation 4}$$

$$Relative\ density\ of\ the\ part\ walls = \frac{Archmedis\ density\ of\ the\ part\ walls}{Estimated\ HAp\ feedstock\ density} \times 100$$

Equation 5

$$Total\ porosity = 100 - \left(\left(\frac{\left(\frac{Dry\ mass\ of\ the\ part}{Total\ part\ volume}\right)}{Estimated\ HAp\ feedstock\ density}\right) \times 100\right) \qquad \textbf{Equation 6}$$

Minitab software was used to perform analysis of variance (ANOVA), regression model fitting, and Taguchi analysis to plot main effects plot and identify the most contributing process parameter that affects CF^3 3D printed parts response parameters such as layer thickness, bead width, surface roughness, and volume fraction of part filled.

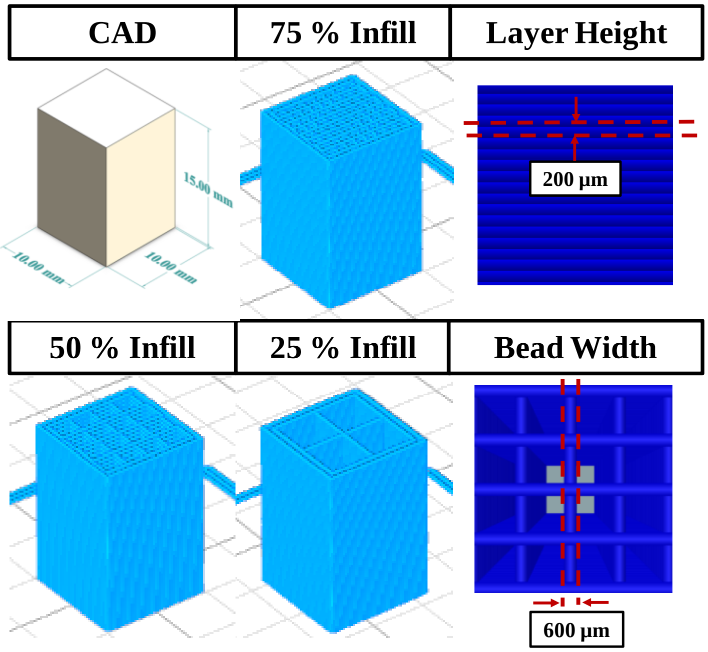

Figure 1. Part CAD geometry designed in SolidWorks (L×W×H of 10×10×15 mm) with sliced geometries of 75 %, 50 % and 25% infills used for 3D printing. Representative images for layer thickness and bead width set while slicing the 3D CAD model.

The ANOVA analysis results were further used to determine the ranking of each CF^3 process parameter for each response parameter measured. Using the percent contribution calculations, the ranking of each process parameter was decided. **Equation 7** was used to identify the percent contribution of each DOE process parameter.

$$\%Contribution = \frac{Adj.Sum\ of\ Squares}{Total} * 100 \qquad \textbf{Equation 7}$$

2.3 Results and Discussion

2.3.1 Material Characterization and CF^3 Parts

The SEM micrograph of the HAp powder is shown in **Figure 2a**. The HAp powder true density of 2.48 ± 0.002 g/cm^3 and polymer binder density of 0.980 ± 0.002 g/cm^3 was measured using a gas pycnometer. The HAp powder loading for the 63 wt.% feedstock was calculated (**Equation 1**) to be 45 vol.% and the remaining 55 vol.% was polymer binder. **Figure 2b** shows typical mixing torque variation as a function of missing time recorded during preparing the 63 wt.% (45 vol.%) HAp powder-polymer binder feedstock. The polymer binder component was first added to the torque rheometer mixing bowl allowing it to melt and upon the addition of HAp powder the mixing torque initially increased to about 120 Nm followed by a decrease and stabilization as the powder-polymer mixture is homogenized. The mixing was performed for 45 min and a stable plateau region was observed in the mixing torque indicating homogenous mixing of the HAp powder-polymer binder feedstock. Subsequently, HAp filaments were extruded using this feedstock for performing 3D printing experiments.

Four cuboid parts, with various infill %, using the conditions listed in **Table 1** were *CF^3* 3D printed for each DOE experiments conditions as shown in **Figure 3**. From **Figure 3** it can be observed that the part printing was successful, and the parts have no visible defects with good shape retention. Additionally, four 100% infill cuboid parts were also printed that served as a reference for performing volume comparisons. **Figure 3** also shows the top and side views of the printed parts. The only visible difference among the samples is the number of square openings, which increased with increasing the infill from 75% to 25%. Each DOE experiment (**Table 1)** represents a different set of printing conditions and therefore, it is expected that these parameters would result in some measurable changes in the surface roughness, bead width, layer thickness, and printed part volume. We have performed detailed ANOVA and regression analysis to understand these influences.

The HAp 3D printed parts were characterized by optical microscopy by measuring layer height and bead width at three different locations on the part. **Figure 4** shows representative images of bead width and layer thickness for CF^3 3D printed HAp parts printed using different print parameters. While 3D printing the bead width was kept constant at 600 µm but measured bead widths on printed HAp parts were always higher than the set value. As it can be seen from **Figure 4** that the best possible measured bead width was ~650 ± 50 µm for DOE 1 while the worst possible measured bead width was for 1030± 30 µm for DOE 7.

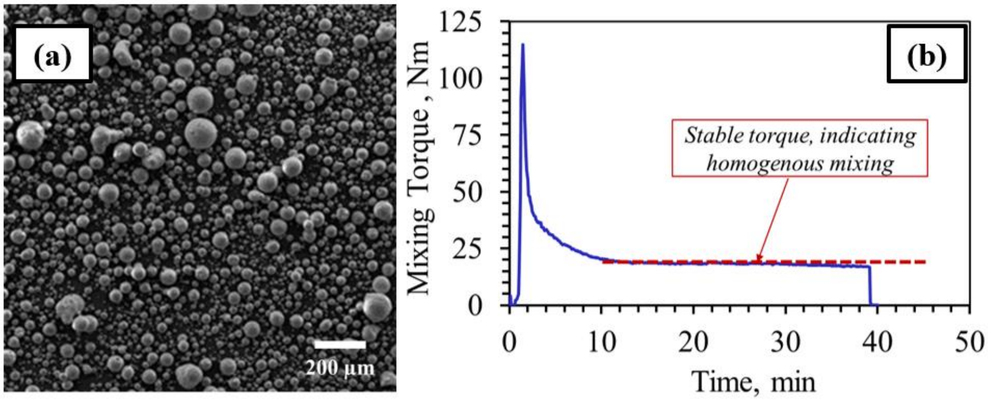

Figure 2. HAp powder and feedstock characteristics a) SEM image of HAp powder showing their spherical shape and (b) stabilization of mixing torque with mixing for HAp powder polymer feedstock compounded at 75 wt.%.

In the case of layer thickness which was set constant at 200 µm when 3D printing the measured layer thickness on printed HAp parts was comparatively closer to the set value. As it can be seen in Figure 4 that the average layer thickness for DOE 1, 6, and 7 was between 190 and 235 µm. A more detailed analysis on the variations observed in bead widths and layer thicknesses are discussed in subsequent sections.

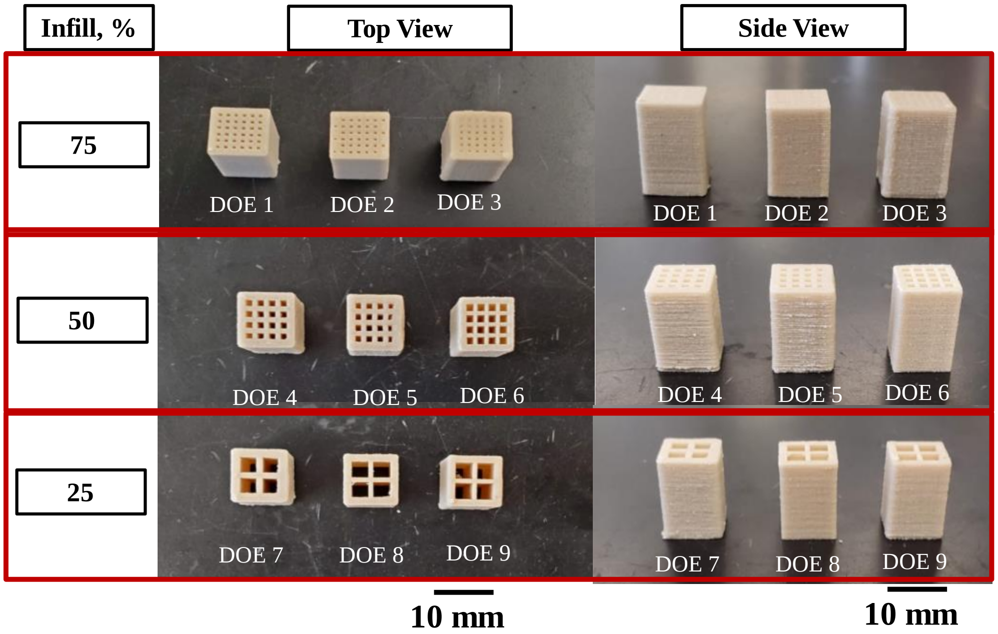

Figure 3. Representative CF^3 3D printed HAp parts printed using different print parameters.

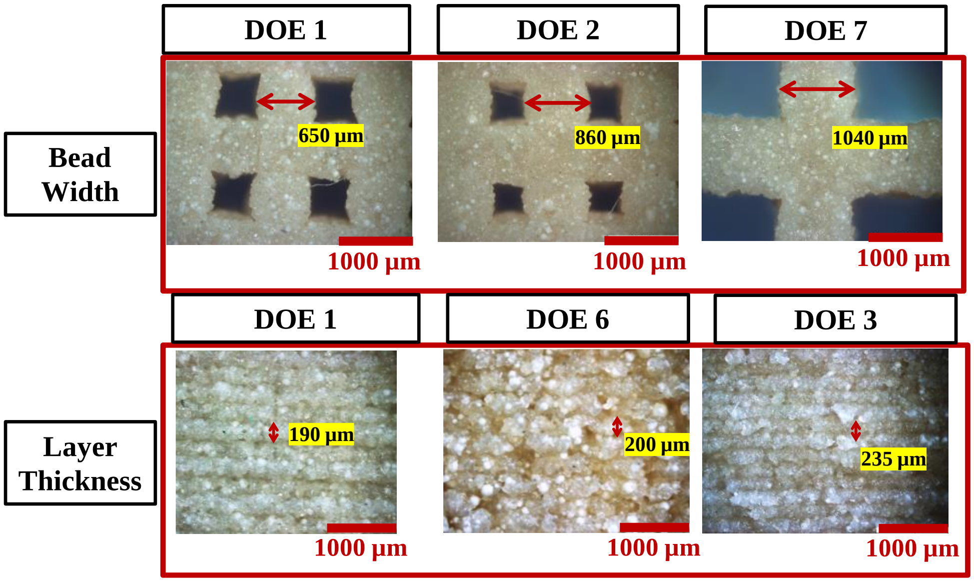

Figure 4. Representative images of bead width and layer thickness for CF^3 3D printed HAp parts printed using different print parameters.

2.3.2 Influence of Printing Parameters on the Layer Thickness

To investigate the effect of 3D printing process parameters such as print speed, extrusion multiplier, and infill% to achieve expected layer thickness, optical microscope images of the printed parts, along the build direction, were taken as shown in **Figure 4**. The layer thickness along the 3D printing build direction was measured from these images and at least 3 images were used for each sample. **Figure 5a** shows the layer thickness thus measured for each DOE experiment. All parts showed higher layer thickness than the set 200 µm values expect for parts printed with DOE conditions 1 and 6. The experimentally measured layer thickness of DOE 1, 2, 4, 6, 8, and 9 process conditions varied between 200 and 210 µm. However, 3, 5 and 7 DOE experiments resulted in thicker layers of > 230 µm, which is attributed due to a high extrusion multiplier of 1.2 and higher print speeds which can result in more material depositing per unit area and time resulting in more expansion of printed layers with not sufficient solidification before the next layer gets printed. This can be related to the thermal (specific heat, thermal conductivity, and coefficient of thermal expansion) and rheological (viscosity as a function of temperature and shear rate) properties as indicated in prior work[14]. Overall, with extrusion multiplier of 0.8 and 1 a.u. can result in achieving the desired layer thickens when printing with high solid loading 63 wt.% HAp filaments. To further understand effect of each process parameter on influencing layer thickness Taguchi, and ANOVA analysis was performed.

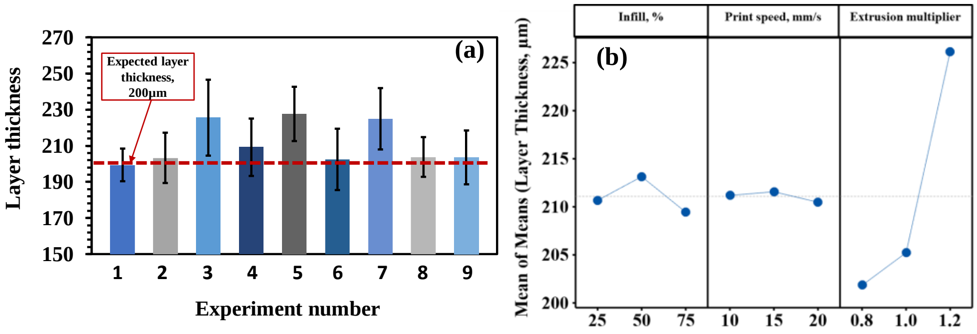

Figure 5. Effect of printing parameters on the layer thickness of CF^3 3D printed HAp parts (a) experimentally measured layer thickness and b) main effects of printing parameters on the layer thickness of CF^3 processed HAp parts.

Taguchi and ANOVA analysis was performed using the measured layer thickness values to identify the individual effect of printing parameters on the layer thickness. **Equation 7** was used to calculate % contribution and subsequently rank each process parameter. **Table 2** provides results from the ANOVA analysis conducted and % contribution calculations.

The highest contribution was identified as extrusion multiplier with 97 % while infill % and print speed had less than 2% contribution that influenced layer thickness. **Figure 5b** shows the main effects plots of printing parameters on the mean of means for layer thickness. It can be observed from **Figure 5b** that among the parameters studied in this investigation extrusion multiplier had the strongest influence and the layer thickness increased with increasing extrusion multiplies. However, the infill % and print speed were found to have a relatively small influence. Additionally, with an increase in extrusion multiplier the mean of means for layer thickness increases. This result is in accordance with the observations made in **Figure 5a** that extrusion multiplier of 1.2 resulted in printing a thicker layer of ~230 µm. A possible reason for this behavior is that with increase in extrusion multiplier more material is extruded out of the nozzle which increases the layer thickness. Overall, an extrusion multiplier of 0.8 a.u. resulted in achieving a layer thickness close to the set value of 200 µm whereas any variation of infill % and print speed resulted in the mean layer thickness to be around 210 µm which is still within ±20 µm resolution of the 3D printer used in the current study.

Table 2. ANOVA analysis and % contribution for layer thickness, bead width, surface roughness parallel (‖) and perpendicular (⊥) to the 3D printing direction, infill % and relative density

Response Type	Factors	Degrees of freedom	Sum of squares, SS	Adjusted mean squares, Adj MS	F-Value	P-Value	% Contribution
Layer thickness	**Infill %**	2	21	11	1.46	0.41	2%
	Print speed	2	2	1	0.13	0.89	0%
	Extrusion multiplier	2	1036	518	71.41	0.01	97%
	Error	2	15	7			
	Total	8	1074				
Bead width	**Infill %**	2	12420	6210	2.46	0.29	9%
	Print speed	2	18649	9324	3.69	0.21	14%
	Extrusion multiplier	2	95149	47574	18.83	0.05	72%
	Error	2	5054	2527			
	Total	8	131272				
Surface roughness (⊥)	**Infill %**	2	3	1	9.89	0.09	11%
	Print speed	2	2	1	8.31	0.11	9%
	Extrusion multiplier	2	22	11	74.17	0.01	79%
	Error	2	0	0			
	Total	8	27				
Surface roughness (‖)	**Infill %**	2	4	2	3.43	0.23	30%
	Print speed	2	8	4	7.10	0.12	62%
	Extrusion multiplier	2	0	0	0.01	0.99	0%
	Error	2	1	1			
	Total	8	13				
Infill %	**Infill %**	2	1064	532	1575.69	0.00	81%
	Print speed	2	20	10	29.02	0.03	1%
	Extrusion multiplier	2	231	115	341.53	0.00	18%
	Error	2	1	0			
	Total	8	1315				
Relative density	**Infill %**	2	1	0	0.35	0.74	11%
	Print speed	2	2	1	0.76	0.57	23%
	Extrusion multiplier	2	3	1	1.19	0.46	36%
	Error	2	2	1			
	Total	8	8				

2.3.3 _Influence of Printing Parameters on the Bead Width

To investigate the influence of printing parameters on the bead width optical images were taken to measure bead width at three different sections on top and bottom of the part. Representative images for bead widths are shown in **Figure 4** that show best, average, and worst cases. For CF^3 3D printing, the bead width was automatically calculated by Simplify3D software as 600 µm. **Figure 6a** shows the bead width measured for each DOE experiment and it can be observed that DOE 1, and 6 process conditions resulted in the bead width being between 600 and 650 µm which is the closest possible bead width of 600 µm. However, DOE experiments 2-5, 8, and 9 resulted in printing bead widths between 660 and 840 µm while DOE experiment 7 resulted in the highest bead width of 1000 µm. It can be observed from **Table 1** and **Figure 6a** that increasing the print speed can decrease the width due to less amount of material being extruded per unit time at any place on the build plate, which results in the less lateral spread and therefore the width of the printed beads will be less. An ANOVA analysis was further conducted to identify the influence of each process parameter on bead width of the printed part as shown in **Table 2**.

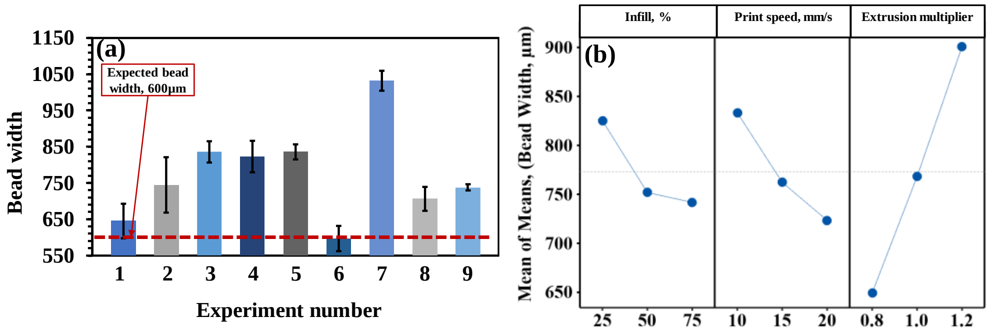

Figure 6. Effect of printing parameters on the bead width of CF^3 3D printed HAp parts (a) experimentally measured bead width and b) main effects of printing parameters on the bead width of CF^3 processed HAp parts.

The highest contributing factor that affected bead width was the extrusion multiplier with 72% contribution followed by the print speed with 14% contribution as shown in **Table 2**. **Figure 6b** shows the main effects plots of the mean of means plotted for bead width as a function of infill %, print speed, and extrusion multiplier. It can be observed from **Figure 6b** that the main effects plot of mean of means for bead width shows that with an increase in extrusion multiplier from 0.8 to 1.2 a.u. the mean of means bead width increased from 650 to 900 µm. A possible reason for such a behavior can be attributed to more material getting deposited with an increase in extrusion multiplier that spreads laterally increasing the effective bead width. In the case of infill % and print speed, a decrease in bead width was observed with their increase. As observed in DOE 1 and 6 in Figure 6a, that a combination of extrusion multiplier of 0.8 a.u. and print speed of 10 and 15 mm/s respectively resulted in achieving mean bead width of ~650 µm which was closest to the set bead width of 600 µm. This behavior indicates that at the lowest extrusion multiplier of 0.8 a.u. bead width can be controlled to a certain extent by extruding less material per unit area and time. Overall, an extrusion multiplier of 0.8 a.u. resulted in achieving desired bead width whereas the highest print speed of 20 mm/s resulted in the lowest possible mean bead width of around ~700 µm. However, when a print speed of 20 mm/s is coupled with an extrusion multiplier of 0.8 a.u. can result in achieving the expected bead width when printing with high solid loading 75 wt.% HAp filaments.

2.3.4 Surface Roughness Analysis for the CF^3 3D Printed Parts

To investigate the effect of changing 3D printing process parameters such as print speed, extrusion multiplier, and infill% that resulted in the lowest surface roughness, measurements of surface roughness were performed ∥ and ⊥ to the printed surface. **Figure 7** shows the Taguchi analysis performed on the measured surface roughness to identify the most contributing process parameter affecting it. Additionally, **Table 2** provides results from the ANOVA analysis conducted and % contribution calculations.

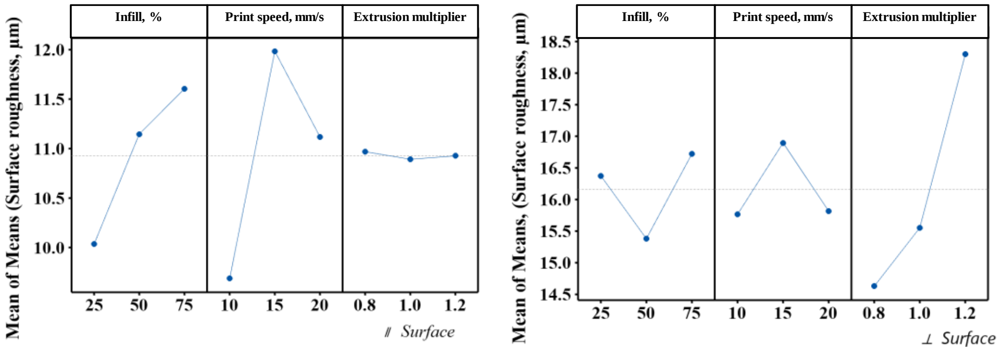

Figure 7. Effect of printing parameters on the surface roughness of CF^3 3D printed HAp parts with main effects plot of mean of means plotted for surface roughness a) ∥ to the printed surface and b) ⊥ to the printed surface of CF^3 processed HAp parts

Figure 7a shows the main effects plots of the mean of means plotted for surface roughness ∥ to the printed surface as a function of infill %, print speed, and extrusion multiplier. It can be observed from **Figure 7a** that the main effects plot of mean of means for extrusion multiplier shows the lowest change while print speed and infill % show the highest change. However, the total change observed is negligible and is between 10 and 12 µm. Similarly, % contributions of print speed showed the highest contribution of 64 % followed by infill % as indicated in **Table 2** and these observations match closely with the trends observed in **Figure 7a**. **Figure 7b** shows the main effects plots of mean of means plotted for surface roughness ⊥ to the printed surface as a function of infill %, print speed, and extrusion multiplier. It can be observed from **Figure 7b** that the main effects plot of mean of means for extrusion multiplier shows the highest change from 4 µm while print speed and infill % show the minimal change. However, the total mean surface roughness ~16 µm for ⊥ to the printed surface is higher than the mean surface roughness of 11 µm observed for ∥ to the printed surface. Conversely, the extrusion multiplier seems to show the highest contribution of 79% that affects surface roughness as observed in **Table 2** and a similar trend was observed in **Figure 7b** for extrusion multiplier. Such behavior indicates that as more material is extruded by increasing extrusion multiplier it can create rougher surfaces due to more material spreading laterally than desired bead widths.

2.3.5 Infill % Analysis for the CF^3 3D Printed Parts

The experimental infill % was calculated using **Equation 2 – Equation 6** and further compared with designed infill % as shown in **Figure 8a**. For CF^3 HAp 3D printing DOE experiments, a cuboid with 10 x 10 x 15 mm was taken as reference and parts were printed with print infill of 75, 50 and, 25% fraction filled with HAp. **Figure 8a** shows the experimental infill % measured for each DOE experiment compared with designed infill % and it can be observed that except for DOE 1 all the other experiments resulted in printing parts with higher infill %. Potential reasons for such behavior can be attributed to increase in bead width and layer thickness than expected as observed in **Figure 5** and **Figure 6.** To further understand how each printing process parameter such as infill %, print speed, and extrusion multiplier affected infill % printed an ANOVA analysis was performed to identify their contributions as shown in **Table 2.**

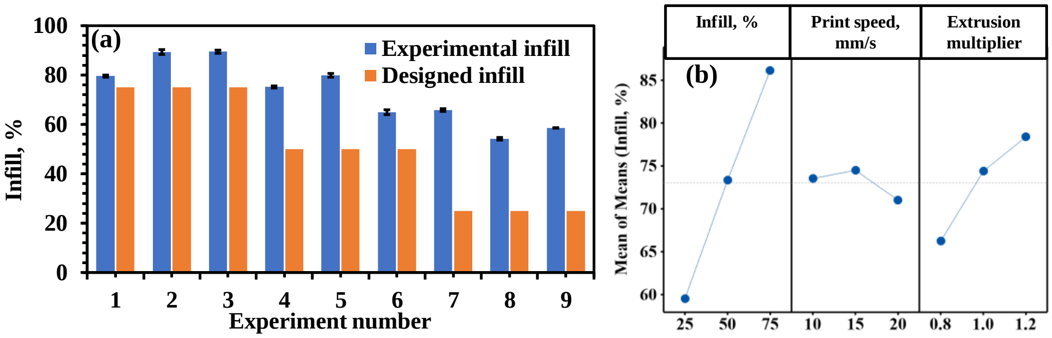

Figure 8. Effect of DOE on infill % filled of the 10mm x 10 mm x 15 mm cuboid filled for CF^3 3D printed HAp parts with a) experimental and designed infill % of cuboid filled for each DOE experiment and b) main effects plot of mean of means plotted for infill % of cuboid filled of CF^3 processed HAp parts.

The ANOVA analysis results in **Table 2** indicate that the infill% manifested 81% contribution followed by extrusion multiplier by 18%. This means that as less volume of material needs to be filled there is more control in printing parts with expected infill % however as the infill % is increased from 25 to 75 there is more material that gets filled due to a combination of overprinting caused by an increase in layer thickness and bead width. This result can be due to increase in extrusion multiplier that causes more volume of material getting printed that directly changes the volume of part to be printed. Additionally, Taguchi analysis was performed on the measured printed part volume values to identify the most contributing process parameter that affects layer thickness. **Figure 8b** shows the main effects plots of mean of means plotted for printed part volume fraction observed as a function of infill %, print speed, and extrusion multiplier. It can be observed from **Figure 8b** that the main effects plot of mean of means for extrusion multiplier and infill % shows the highest change and more fraction filling was observed with their increase. However, print speed variation showed no noticeable change.

2.3.6 Relative Density Analysis for the CF^3 3D Printed Parts

Relative density for HAp printed parts was measured using Equation 5 and plotted in Figure 9a and an ANOVA analysis was performed to identify process parameter which influences relative density the most as shown in **Table 2**. It can be observed from **Figure 9a** that DOE 1-3 have a relative density of ~85-87% as shown in **Figure 8a**. Similarly, for DOE 4-6 the relative density of parts was observed to be ~86-88% and for DOE 7-9 the relative density was between ~85-87% as shown in **Figure 9a**. This indicates that the walls of the parts have closed porosity of about 12-15% than expected. The ANOVA analysis performed for identifying influence of each process parameter affecting relative density as shown in **Table 2** revealed that the extrusion multiplier showed the most significant contribution of 34% followed by infill % and print speed.

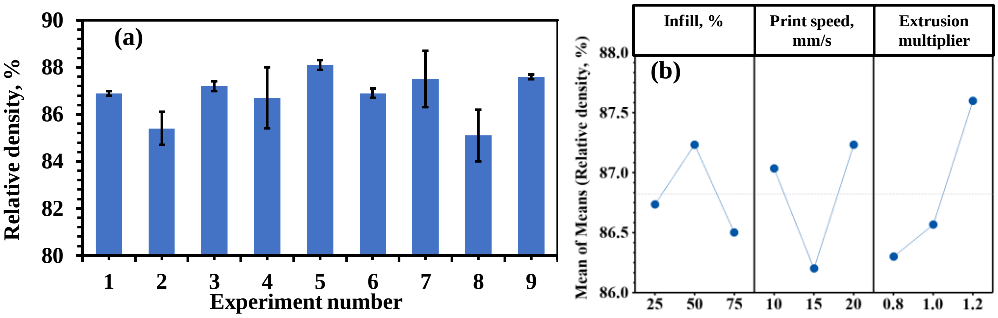

Figure 9. Effect of DOE on relative density of CF^3 3D printed HAp parts with a) relative density for each DOE experiment and b) main effects plot of mean of means plotted for relative density of CF^3 processed HAp parts.

Taguchi analysis was performed for relative density and the main effects plot for mean of means was plotted in Figure 9b. It can be observed that the extrusion multiplier showed the highest contribution, and no clear trend was observed for infill % and print speed. This result is comparable to what was observed in ANOVA analysis but attaining the highest relative density was with the highest extrusion multiplier of 1.2 a.u. This observation follows the trend observed with the above results for infill%, bead width, and layer thickness that indicate more material flowing out of the nozzle with a higher extrusion multiplier can result in more contact points between beads and layers causing an increase in relative density. However, there is a downside of this trend as it causes parts to be overfilled and not up to specifications.

2.3.7 Regression Analysis for the CF^3 3D Printed Parts

Analysis of variance (ANOVA) was performed for DOE responses of layer thickness, bead width, surface roughness ∥, and ⊥ to the printed surface, volume fraction by generating regression equations. Subsequently, the coefficient of regression (R^2) for obtained regression equation were determined. **Table 3** shows regression equation fitting performed for layer thickness, bead width, surface roughness ∥ and ⊥ to the printed surface, infill %, and relative density. As it can be observed from **Table 3** that all the DOE responses in regression equation have an excellent closeness of fit in their prediction with R^2 ranging between 70 and 99%. The equations provided in **Table 3** enable predicting individual responses when input values for infill %, extrusion multiplier, and print speed are entered.

Table 3. Regression equation for DOE responses of layer thickness, bead width, surface roughness ∥ and ⊥ to the printed surface, infill % and relative density and coefficient of regression (R2) for the regression equation.

DOE Response	Regression Equation	R^2
Layer Thickness	Layer thickness = 211.087 - 0.42 Infill %_25 + 2.05 Infill %_50 - 1.64 Infill %_75 + 0.11 Print speed_10 + 0.49 Print speed_15 - 0.60 Print speed_20 - 9.22 Extrusion multiplier_0.8 - 5.83 Extrusion multiplier_1.0 + 15.05 Extrusion multiplier_1.2	99
Bead Width	Bead width = 773.0 + 52.2 Infill %_25 - 21.1 Infill %_50 - 31.1 Infill %_75 + 60.3 Print speed_10 - 10.8 Print speed_15 - 49.6 Print speed_20 - 123.6 Extrusion multiplier_0.8 - 4.6 Extrusion multiplier_1.0 + 128.2 Extrusion multiplier_1.2	96
Surface Roughness (∥)	Surface roughness (∥) = 10.928 - 0.893 Infill %_25 + 0.218 Infill %_50 + 0.675 Infill %_75 - 1.243 Print speed_10 + 1.053 Print speed_15 + 0.189 Print speed_20 + 0.040 Extrusion multiplier_0.8 - 0.037 Extrusion multiplier_1.0 - 0.003 Extrusion multiplier_1.2	91
Surface Roughness (⊥)	Surface roughness (⊥) = 16.159 + 0.216 Infill %_25 - 0.779 Infill %_50 + 0.563 Infill %_75 - 0.395 Print speed_10 + 0.736 Print speed_15 - 0.342 Print speed_20 - 1.531 Extrusion multiplier_0.8 - 0.606 Extrusion multiplier_1.0 + 2.137 Extrusion multiplier_1.2	99
Infill, %	Infill, % = 73.011 - 13.478 Infill %_25 + 0.322 Infill %_50 + 13.156 Infill %_75 + 0.522 Print speed_10 + 1.489 Print speed_15 - 2.011 Print speed_20 - 6.778 Extrusion multiplier_0.8 + 1.389 Extrusion multiplier_1.0 + 5.389 Extrusion multiplier_1.2	99
Relative Density, %	Relative Density, % = 86.822 - 0.089 Infill %_25 + 0.411 Infill %_50 - 0.322 Infill %_75 + 0.211 Print speed_10 - 0.622 Print speed_15 + 0.411 Print speed_20 - 0.522 Extrusion multiplier_0.8 - 0.256 Extrusion multiplier_1.0 + 0.778 Extrusion multiplier_1.2	70

2.4 Summary

HAp powder-polymer feedstock and filaments of 63 wt.% solids loading were successfully fabricated and CF^3 3D printed into desired cuboid geometry. The design of experiments and ANOVA analysis performed on measurements of layer thickness, bead width and volume infill % filled revealed that the most significant contributor that dictates printing to achieve expected layer thickness, bead width and volume infill % filled was extrusion multiplier followed by print speed. This behavior indicates that achieving control over the volume of material extruded per unit area and time governs the geometrical tolerances of CF^3 3D printed HAp parts. In the present work, an extrusion multiplier of 0.8 a.u. and print speed of 10 or 15 mm/s were found to result in parts with high geometrical accuracy. Surface roughness measured parallel to printed beads (∥) was much lower (~11 µm) than the surface roughness in normal (⊥)direction (~ 15 µm). Increasing the extrusion multiplier increased the surface roughness in ⊥ printed direction, which indicates over extrusion of material leading to rougher surfaces. Regression analysis performed on printing process parameters indicates that the models generated had an excellent closeness of fit with R^2 ranging between 90-99, except with relative density which showed R^2 of 70%. Thus, the regression equations can be used to find appropriate process parameters provided input parameters such as print speed, infill %, and extrusion multiplier are provided. This work allows for identifying key printing parameter that influences part quality that is crucial when working with CF^3 3D printing.

CHAPTER 3

PROCESSING OF HYDROXYAPATITE AND ITS COMPOSITES USING CERAMIC FUSED FILAMENT FABRICATION (CF^3)

3.1 Introduction

Processing of ceramics using conventional manufacturing techniques typically involve powder pressing followed by high temperature sintering and machining, as desired. However, machining of ceramics to complex shapes is not only difficult, due to their inherent brittleness, but also causes significant amount of tool wear and material waste. Therefore, advanced manufacturing technologies such as additive manufacturing (AM) have been widely being adopted to manufacture wide variety of ceramic components [10, 21, 22]. The AM technologies that are being used to process ceramics can be grouped as slurry-based (stereolithography, inkjet printing, direct ink writing, digital light processing), powder-bed based (selective laser sintering/melting, binder jetting) and material extrusion-based (fused filament fabrication, robocasting). Although each technology provides unique processing flexibility and capabilities to manuscript complex ceramic parts, ceramic fused filament fabrication (CF^3) is most economical as the machine/equipment, feedstock materials and overall processing cost is relatively lower than other AM processes [22]. Further, the elimination of loose powder and liquid in CF^3 process makes it a best process to manufacture ceramic parts on-demand in space.

Therefore, there is growing interest in this process [23, 24] to manufacture metallic, ceramic and composite parts. In a typical CF^3 process, the powder-binder mixtures, in the form of filament, are extruded through a heated nozzle and deposited on to a heated platform following a pre-determined path to complete a three-dimensional (3D) part. We have recently demonstrated the importance of filaments' material properties in controlling printability, quality and properties of made using this process [23].

Manufacturing of artificial implants to replace natural tissues requires rational combination of biomaterials and processing techniques, to achieve desired functional performance and life under physiological conditions. Since the natural bone inherently have hierarchical variations in the composition and structure it is essential to utilize state-of-the-art capabilities of AM technologies [9, 11]. Among synthetic bioceramics, hydroxyapatite (HAp, $Ca_{10}(PO_4)_6.(OH)_2$) is most popular and is considered as a gold standard for wide variety of bone replacement applications due to its excellent bioactivity and osteoconductivity, that primarily originates from its chemical similarity with natural bone [25]. However, it is inherently brittle and has low fracture toughness in addition to relatively low osteogenic capability compared to natural bone[2]. Additionally, previous studies on HAp substituted with different cations and anions have shown to improve biological properties significantly [4, 26, 27]. While the addition of oxides such as Al_2O_3 [28], ZrO_2 [29, 30], metals [31] and carbon nanotubes [32] found to improve mechanical properties but with concurrent decrease in the overall bioactivity of HAp. Therefore, in this work we have made an attempt to reinforce the HAp with Si_3N_4, which is a promising material with bioactivity and high strength [33, 34]. It was also found that the Si_3N_4, in addition to its non-toxicity [35], can promote osteoblast activity [36]. Interestingly, Si_3N_4 demonstrated to promote new bone formation in the presence of bacteria and completely inhibit bacterial growth [37, 38]. However, the processing of Si_3N_4 requires extremely high temperature (>1700 °C) and pressures (50 to 200 MPa) to achieve high-density parts with reliable mechanical properties [39]. We also expect that any potential formation of SiO_2 layer on Si_3N_4 particles, during high-temperature sintering, could react with HAp leading to the formation of liquid phase thus results in better densification.

Considering simple processing of HAp and bioactivity, high strength of Si_3N_4 a biocomposite containing these two bioceramics can provide artificial bone replacement material with combination of processing flexibility, high strength and bioactivity. Further, the use of CF^3 enable fabrication of complex bioactive ceramic implants with potentially superior functional and mechanical performance compared to current bioactive ceramic implants. Therefore, in this investigation we aim to understand the processing and microstructures of pure HAp and HAp + 10 wt.% Si_3N_4 samples using CF^3. The feedstock and printed samples were characterized in terms viscosity, extent of binder removal, surface topography, porosity, shrinkage, phase analysis and microstructural evolution.

3.2 Materials and Methods

Hydroxyapatite (HAp) powder with D_{50} = 25 μm, and Si_3N_4 powder (AlzChem Group AG, Germany) with D_{50} = 2.1 μm were used to prepare HAp feedstock containing 0 and 10 wt.% Si_3N_4. Measured quantities of powder and multi-component binder were loaded in to mixing chamber of a torque rheometer (Intelli-Torque Plasti-Corder, C. W.

Brabender Instruments, Inc. NJ, USA) and mixed (50 RPM) for 20 min. at 180°C to achieve homogenous mixture of binder and powder. It is understandable that high powder loading (often > 80 wt.%) in the feedstock is desirable to achieve high strength filaments and to eliminate slumping and shrinkage during debinding and sintering, respectively. However, our initial blending experiments with solid loading > 80 wt.% resulted in excessively high mixing torque. Further, excessively high powder loading in the filament can also result in high melt viscosity, which is detrimental to the consistent material flow during CF^3. Therefore, we have reduced the powder loading to 63 wt.% in our powder-binder feedstock mixtures, which were crushed into small granules (1 to 5 mm) and then extruded using capillary rheometer (Rheograph 20, GÖTTFERT Werkstoff-Prüfmaschinen GmbH, Germany) to make filaments (∅ 1.75 mm) for CF^3. The filament extrusion was performed at 140°C with 0.10 mm/s speed (shear rate = 33.6 s^{-1}) using a tungsten carbide die (L/D = 30:1) and the viscosity of different feedstocks was also measured to understand the influence of adding Si_3N_4 to HAp on the flowability of binder-powder mixture. The green density of the filaments (n = 10) was measured using Archimedes' principle.

Based on several experiments using desktop FFF machine (Makergear M3, MakerGear LLC, Beachwood, OH, USA) we found that the material flow was inconsistent and resulted in severe nozzle clogging during printing when the extrusion temperature was below 240 °C. Similarly, good adhesion between the part and the build plate was observed when the build platform temperature was 75 °C. Thus, the printing parameters selected to build disc samples (∅ 15 mm; 6 mm thick) in this investigation are presented in **Table 4**. A two-step debinding was used to remove binder from the printed samples. Initially the printed parts were immersed in n-heptane solution at 64 °C for 8 h followed by overnight drying at 80°C. Then the samples were examined for amount of binder removal. Subsequently, final thermal debinding was performed based on the thermal degradation data of the feedstock determined using thermogravimetric analyzer (TGA, SDT Q600, TA Instruments, New Castle, DE, USA). The thermal debinding was followed by a sintering of the samples at 1250 °C for 4 h in a tube furnace (CM Furnaces, Bloomfield, NJ, USA). The shrinkage and density of the sintered samples were determined following standard procedures.

The surface roughness of the sintered samples was determined using a roughness tester (Surftest SJ-210, Mitutoyo America Corporation, OH, USA) and on each sample 5 mm scans at 0.5 mm/s speed were used. The surface roughness of the samples was determined along and across the printed beads. The top surface morphology of as-sintered samples was examined using scanning electron microscope (SEM, TESCAN USA, Inc., Warrendale, PA, USA) to understand the surface topography, printing induced defects and porosity. The sintered samples were sectioned and polished following standard metallographic sample preparation procedure. Then the microstructures of the sintered samples were examined, parallel and normal to the build direction, using SEM. The polished sections of the samples were etched using 30% phosphoric acid for 10-30 s to reveal microstructures. The compositions of different microstructural features were also analyzed using energy-dispersive spectrometer (EDS). Similarly, the constituent phases present in the sintered samples were determined using X-ray diffraction (XRD, Discovery

D8 HR, BRUKER AXS, Inc., USA). Microhardness of the sintered samples was measured using Vickers microhardness tester (W4303, ESEWAY, UK) at 100 g load for 15s.

Table 4. Characteristics of HAp and HAp10SN feedstocks, microhardness of sintered samples and CF3 parameters used in this work. || Parallel to beads, ⊥Normal to beads.

Material	**Viscosity, Pa.S**	**Green filament density, %**				**Roughness (Ra), µm**	
						||	⊥
HAp	21500 ± 443	97 ± 1.0				7 ± 1.0	19 ± 1.8
HAp10SN	22580 ± 861	96 ± 0.6				5 ± 0.8	11 ± 0.9
Sintered Properties							
	Microhardness, HV	**Grain size, µm**					
HAp	81 ± 13	7.5 ± 1.8					
HAp10SN	384 ± 148	2.2 ± 0.98					
FFF printing parameters							
Layer thickness	**Printing speed**	**Printing temperature**	**Bed temperature**	**Nozzle diameter**	**Fill angle**	**Extrusion multiplier**	**Infill**
200 µm	10 mm/s	240 °C	75 °C	500 µm	+5°	1.15	100%

3.3 Results and Discussion

The powder used to prepare present samples was found to have different morphologies, as shown in **Figure 10 (Top)**. The HAp powder had spherical morphology and large variation in the size of the powder. Close observation of HAp powder indicated that the powder was made using spray drying process. However, the Si_3N_4 powder appears to be agglomerated due to its finer size. Further, the powder shape appears to be irregular and angular. The powder attributes such as size and shape have strong influence on the powder-binder mixture properties particularly the viscosity and flowability. In general, finer and irregular powder increases the viscosity of powder-binder mixture due to inter-particle friction and binder flow restriction by these powders [40]. Our experimentally measured viscosity of HAp feedstock, during filament extrusion, increased marginally from HAp 21500 ± 443 Pa.S to 22580 ± 861 Pa.S when 10 wt.% Si_3N_4 was added. Regardless of large variation in the viscosity of HAp10SN feedstock the filaments exhibited relative density close to that of HAp, as shown in **Table 4**. Both filaments found to have relative density between 96 and 97%, which is reasonably good to enable printing. For example, high green density of filaments provide sufficient strength and stiffness to them which is necessary to overcome the pressure drop in the print nozzle thus enabling smooth printing with consistent material flow [41] . Further, in addition to appropriate printing parameters, the use of high-density feedstock filaments is one of the prerequisites to produce high-density parts. For example, post-printing processes such as polymer binder removal by debinding and densification by sintering, are strongly dependent on the green density of printed parts as any pores/ defects present in the filament could prove to be detrimental to the sintered part properties. In line with these statements, the relative density of green parts produced using these filaments and print parameters shown in **Table 4** found to be 93.2 ± 0.2 % and 92.6 ± 0.6 % for HAp and HAp10SN, respectively. Typical CF^3 processed green part is shown in **Figure 11a**.

Thermogravimetric analysis (TGA) of developed feedstock is shown in **Figure 10 (Bottom-left)**, which revealed three distinct peaks (weight loss rate vs temperature) around 250 °C, 330 °C and 440 °C, which correspond to the removal of three components of our polymer binder. Additional broad peak around 700 °C is attributed to the elimination of hydroxyl groups (-OH) from the HAp [42]. The plasticizer reduces feedstock viscosity enabling powder loading and easy printing during CF^3. The elastomer is responsible for filament flexibility and the backbone polymer ensures desired strength and stiffness to the filament. Based on this data thermal debinding cycle was developed, which is presented in **Figure 10 (Bottom-right)**. A hold time of 3 h at 250 °C, 330 °C and 6 h at 440 °C was used for thermal debinding in N_2 atmosphere to ensure complete binder removal from the green parts. Final sintering was carried out in air at 1250 °C for 4 h.

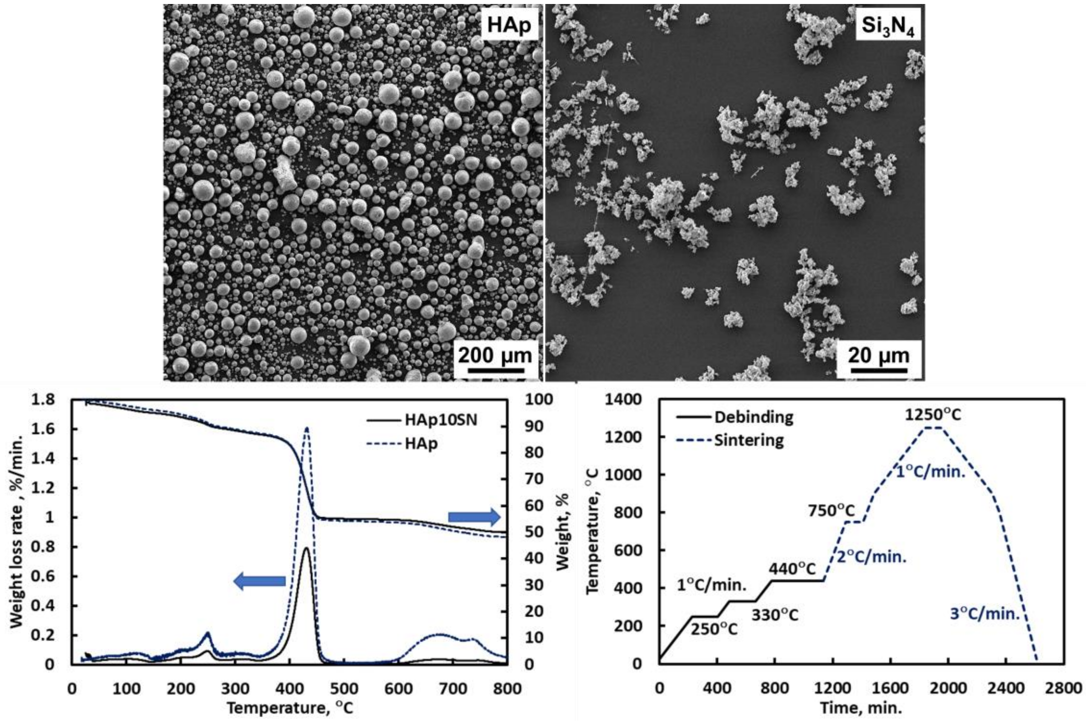

Figure 10. (Top) SEM microstructures showing the morphology and size distribution of HAp and Si3N4 powder used to prepare HAp and HAp10SN samples through CF3. **(Bottom-left)** TGA showing removal of different components of binder used to prepare feedstock for CF^3. **(Bottom-right)** Thermal debinding cycle designed based on TGA data and sintering cycle used to achieve dense HAp and HAp10SN composites.

After solvent debinding in n-heptane (64 °C for 8 h) the HAp samples exhibited 48% binder removal, while the HAp10SN samples showed a binder loss of 59%, as shown in **Figure 11b**. The high amount of binder loss in HAp10SN samples can be attributed to the loss of some Si_3N_4 powder due to its finer size. After final sintering (1250 °C, 4 h) both the samples showed complete removal of binder determined using weight loss measurements. Present CF^3 processed samples were found to retain their shape after sintering without any gross defects such as cracks, delamination, **Figure 11a**, and showed considerable amount of shrinkage, **Figure 11b**. The linear and volumetric shrinkage of the samples was determined to be ~ 30% and 67%, respectively. The addition of Si_3N_4 appears to have no measurable influence on the densification of HAp under present experimental conditions. The relative density of these samples varied between 85 and 86%, shown in **Figure 11b**. The low densification of sintered samples is a direct consequence of low solid loading in the feedstock (63 wt.%). Further improvement in the density of present samples, consequent reduction in shrinkage as well, can be achieved by increasing the powder loading in the feedstock and also by increasing the sintering time. However, increasing the sintering temperature beyond 1250 °C can lead to complete transformation of HAp to tricalcium phosphate (TCP). Similarly, our initial trails with high powder loading resulted in excessively high mixing torque and therefore, we believe that using powder with different powder characteristics such as size and shape, especially Si_3N_4 could enable achieving high sintered density depending on the specific site of implant application. Nonetheless, the presence of porosity in the CF^3 processed HAp and HAp10SN samples is beneficial for proposed bone replacement applications where enhanced osseointegration along with bioactivity is required.

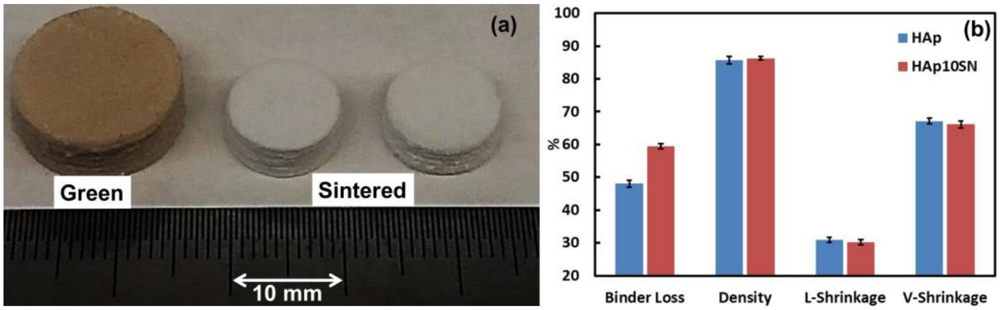

Figure 11. (a) Photograph showing the extent of typical shrinkage after sintering of CF3 processed HAp10SN composites. (b) Amount of binder removed during solvent debinding and the influence of Si3N4 on the relative density and shrinkage of CF3 processed ceramic samples sintered at 1250°C, 4h. L-Shrinkage: linear shrinkage; V-Shrinkage: volumetric shrinkage.

The top surface of as-sintered HAp and HAp10SN samples was observed using SEM to understand the densification, changes in the surface morphology and printed beads. It can be seen from **Figure 12** that both the samples have clear print beads (dotted lines), which were relatively rough in HAp samples compared to those found on HAp10SN samples. Moreover, the bead-to-bead interface appeared to be overflown in the HAp samples. This overflow of material, due to lateral flow of printed beads, could be due to lower viscosity of HAp feedstock compared to HAp10SN feedstock at present printing temperature of 240 °C. No printing induced gross defects such as under-fill and bead-dead delamination were found on these samples. However, the amount of porosity also appears to be high in these build-up areas (circles in **Figure 12**) compared to other regions due to less compaction of printed beads. The HAp10SN samples, on the other hand, were relatively smooth with less amount of material build-up between the adjacent beads. These observations were further corroborated by surface roughness measurements performed on these samples, **Table 4**. Average roughness measured normal to the printed beads was 11 ± 0.9 μm for HAp10SN, which is significantly less than that of HAp with 19 ± 1.8 μm. Although small, the roughness along the beads was also different on these two samples.

We also observed some difference in the amount of porosity and surface irregularities across the sample surfaces. The regions near the sample edge (perimeter) revealed relatively high amount of porosity and rough surface topography compared to the central regions of the samples. In the central region, both samples, showed smooth, densified regions (arrows in the insets of **Figure 12**) suggesting good amount of densification. Although the relative density of HAp and HAp10SN samples is same (**Table 4**) the local densification appears to be more in the latter samples, which can be seen from the smooth/densified surface regions with clear grain boundaries (arrows in the insets of **Figure 12**). This suggests that addition of Si_3N_4 can improve sinterability of HAp in the regions surrounding Si_3N_4 particles. However, low amount of powder loading (40 vol.%) in the present feedstock resulted in almost similar amount of total porosity in both samples. We believe that increasing the powder loading can increase the HAp-Si_3N_4 contacts and thus potentially result in uniform densification throughout the bulk leading to high density HAp10SN composites.

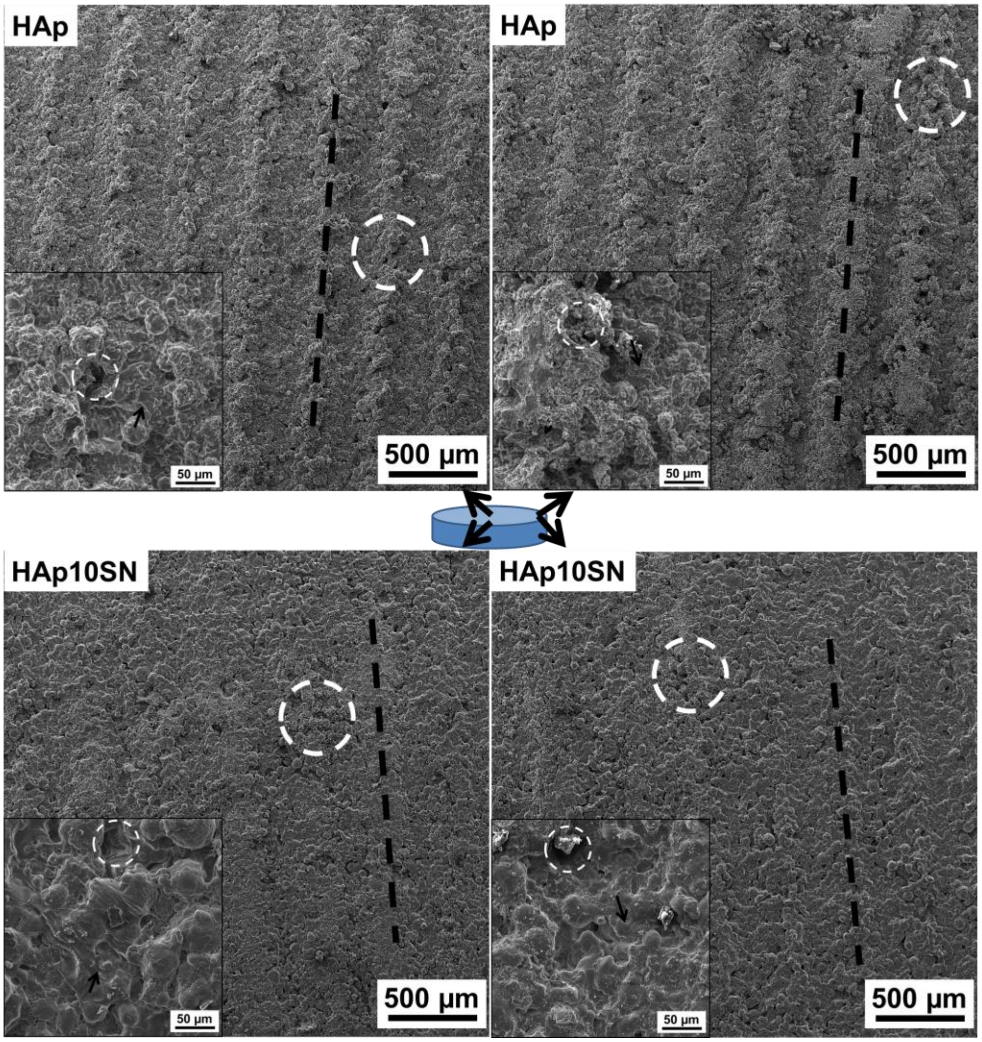

Figure 12. Top surface morphology showing extent of surface roughness and topographical features found on sintered HAp and HAp10SN ceramics. Lines indicate orientation of printed beads and circles shows group of pores. In the insets high-magnification SEM images highlights the dense and smooth areas (arrows).

Sintered HAp and HAp10SN samples were sectioned along the build direction to assess the porosity distribution across the samples. Typical polished sections of the sintered samples are presented in **Figure 13**. Present samples showed isolated pores of ~ 10 μm and interconnected pores in the range of 150 to 200 μm, which are considered ideal of bone in growth [43]. It was observed that the amount of porosity varied across the sample in built direction, as observed on the top surface of these samples (**Figure 12**). Very little amount of porosity was observed in the central region of the samples, which also revealed densified regions. However, the top layers of the samples found to have relatively more amount of porosity compared to the bottom and middle layers. Similarly, the sample edges also exhibited high mount of porosity, particularly in the top layers. The high density in the bottom layers of the samples can be attributable to the dense packing and bonding of beads due to thermal influence of bed temperature (75 °C). During printing, the deposited beads remain at relatively high temperature for longer time in the bottom layers (say 5 to 10 layers) due to bed temperature of 75 °C. As a result, the printed material packs and bonds well in these layers. As the building process continues the influence of bed temperature gradually decreases as the desktop printer used in this investigation do not have temperature-controlled build chamber. Therefore, the packing appears to decrease in the top layers leading to relatively more amount of porosity. Lack of dense packing in the sample edges (top layers) could be due to faster heat dissipation towards free atmosphere, which is relatively less in the central regions. From these observations it can be said that uniform packing and bonding is essential to achieve uniform densification during sintering of CF^3 parts, which can be achieved through adjusting printing parameters for different regions of the parts and using build chamber temperature control.

The microstructures of sintered HAp and HAP10SN samples after chemical etching are shown in **Figure 14**. Clear difference in the microstructural feature size can be seen from these SEM microstructures. Sintered HAp10SN samples revealed irregularly shaped Si_3N_4 particles of different sizes. This indicates that these composites retained Si_3N_4

particles, although some reaction with the HAp matrix could be seen, which resulted in change in the overall shape of the particles. The grain size of pure HAp samples, measured using linear intercept method, was found to be 7.5 ± 1.8 μm. The addition of Si_3N_4 to HAp appears to reduce the grain size significantly and these samples exhibited a grain size of 2.2 ± 0.98 μm, which is ~ 70% reduction. The formation of liquid phase as a result of interaction between Si_3N_4 and HAp matrix is believed to be responsible for this microstructural refinement in HAp10SN samples.

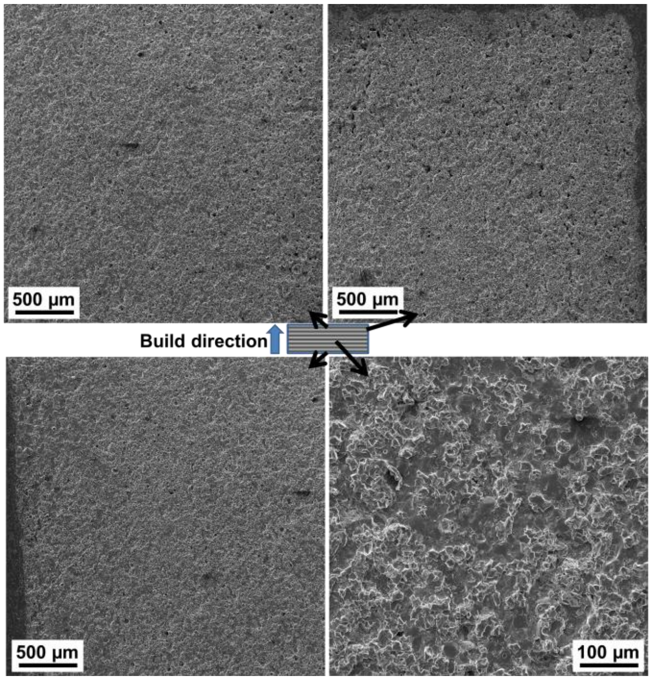

Figure 13. Typical distribution of porosity across sintered ceramics samples made using CF3. Both sample edges and top layers of the samples clearly indicate relatively more amount of porosity compared to the central region and bottom layers of the samples.

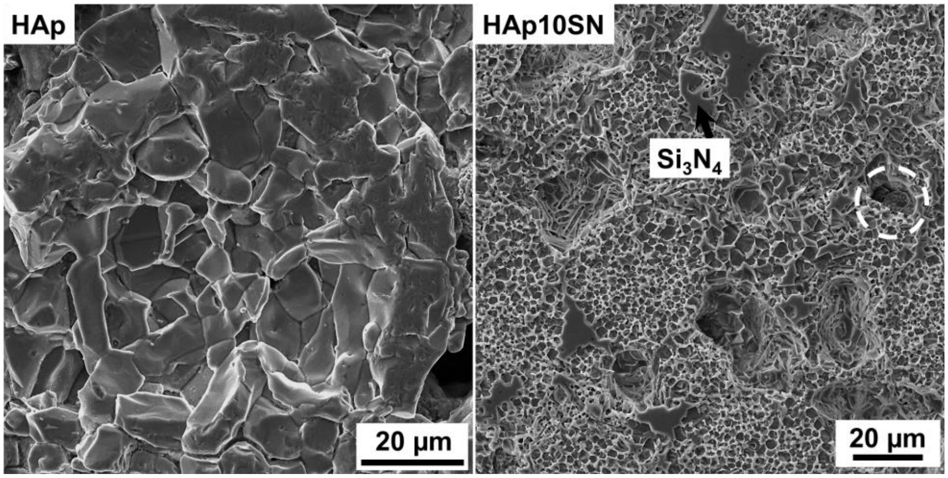

Figure 14. Microstructures of sintered HAp and HAP10SN ceramics showing grain size characteristics and distribution of pores and different phases. Circles indicate residual pores.

The constituent phases of sintered HAp and HAp10SN samples were determined using XRD and the results are shown in **Figure 15**. Both samples showed the presence of HAp and some peaks corresponding to tricalcium phosphate (TCP) were also observed. It appears that partial decomposition of HAp to TCP occurred during sintering of these samples at 1250 °C, which is expected during sintering at temperatures above 1050 °C [42, 44]. The HAp10SN composites showed peaks corresponding to Si_3N_4 suggesting retention of these particles after sintering. It is also expected that sintering in air can lead to some oxidation of Si_3N_4 particles and can form thin SiO_2 layer on these particles, which can potentially assist in densification [45]. We could not identify any peaks corresponding to SiO_2 presumably due to its low concentration. However, it appears that the Si_3N_4 and HAp matrix reacted during sintering and formed small amount of $CaSiO_3$, suggesting the formation of SiO_2 which reacted with HAp to form $CaSiO_3$.

Potential reactions that can results in the formation of different phases in the sintered HAp10SN samples include:

$$Ca_{10}(PO_4)_6(OH)_2 + SiO_2 \rightarrow 3Ca_3(PO_4)_2 + CaSiO_3 + H_2O\ (g)$$ **Equation 8**

$$Ca_{10}(PO_4)_6(OH)_2 \rightarrow 3Ca_3(PO_4)_2 + CaO + H_2O\ (g)$$ **Equation 9**

$$10Ca_3(PO_4)_2 + 2SiO_2 \rightarrow 10Ca_3(P_{0.9}Si_{0.1}O_{3.95})_2 + P_2O_5$$ **Equation 10**

$$(2+3x)Ca_{10}(PO_4)_6(OH)_2 + 2xSiO_2 \rightarrow 10xCa_3(PO_4)_2 + \\ 2Ca_{10}(PO_4)_{6-x}(SiO_4)_{2-x}(OH)_{2-x} + xH_2O\ (g)$$ **Equation 11**

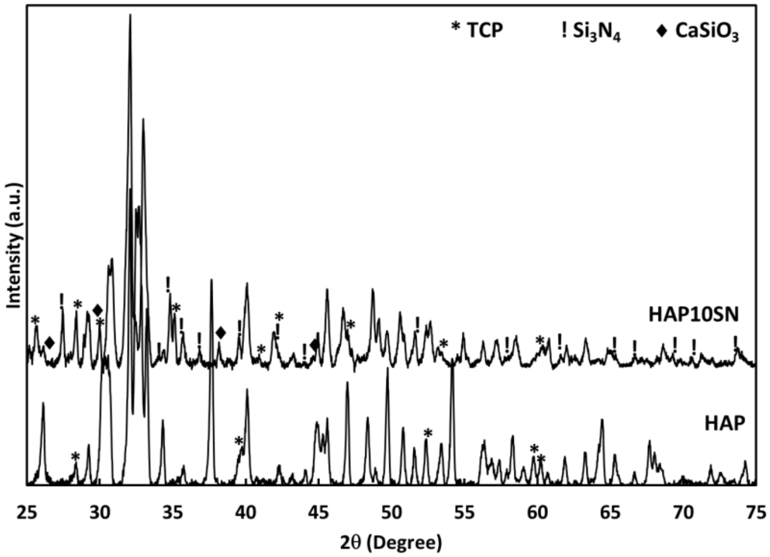

Figure 15. Phase constituents of different samples identified using XRD. Unlabeled peaks correspond to HAp.

At sintering temperature the transformation of HAp [$Ca_{10}(PO_4)_6(OH)_2$] ➔ TCP [$Ca_3(PO_4)_2$] is associated with loss of excess Ca^{2+} ions from HAp [46]. In the presence of Si_3N_4 particles with potential SiO_2 on their surface would result in the formation of TCP and $CaSiO_3$ following **Equation 8** [47]. The presence of $CaSiO_3$ peaks in the XRD spectra of HAp10SN samples (**Figure 15**) indicates that this reaction would have occurred during sintering of these samples. Other potential reaction combination [46] that can lead to the formation of Si substituted TCP and glassy phase is **Equation 9** and **Equation 10**. Simultaneous formation of CaO and P_2O_5 as per **Equation 9** and **Equation 10**, respectively, can result in the formation of glassy phase consisting of Ca-Si-P-O as reported in earlier investigations [46, 48, 49]. Relatively broader and lower diffraction peak intensity of HAp10SN samples compared to HAp indicates the formation of glassy phase in the former samples. The substitution of PO_4^{3-} with SiO_4^{4-} in the HAp could also result in the formation of Si substituted HAp along with TCP following **Equation 11** [50]. These compositional and microstructural modifications, due to Si_3N_4, increased the hardness of pure HAp samples from 81 ± 13 HV to 384 ± 148 HV. However, the microstructural non-uniformity in HAp10SN samples resulted in large variation in the hardness (200-683 HV) across the sample i.e., local densification and reaction with HAp matrix in the regions surrounding Si_3N_4 particles. Nonetheless, minimum of 147% increase in the hardness is notices due to the addition of Si_3N_4 particles to HAp and further reduction in the hardness variation can be achieved by CF^3 processing of these composites with higher solids loading.

To identify different phases and reaction between Si_3N_4 and HAp matrix EDX elemental mapping across microstructural features of sintered HAp10SN ceramic composites was performed. The compositional mapping, shown in **Figure 16,** revealed relatively high concentration of Si and N in the regions of Si_3N_4 particles, which suggests that particles were intact in the HAp matrix after sintering at 1250 °C, 4 h. It is also important to note that in these regions the concentration of Ca and P is significantly less compared to other regions. However, O appears to be present throughout the microstructure, except some isolated regions. Therefore, it can be said that during sintering in air partial surface oxidation of Si_3N_4 particles would have occurred and formed thin SiO_2 layer on these particles. The overall composition of this region was found to have Ca/P ratio of 1.69, which is close to that of HAp.

Additionally, point EDX analysis was used to determine the composition of individual phases shown in **Figure 16** and the results are summarized in **Table 5**. The compositional analysis showed that Si/N ratio (wt. %) of Si_3N_4 particles in the sintered HAp10SN samples increased to 5.42 compared to that of feedstock powder with ratio of 1.59. This suggests that there is some loss of N due to partial surface oxidation of Si_3N_4 particles during high temperature sintering. Similarly, the Ca/P ratio (wt. %) in the matrix was measured to be 1.496 which is less than that of HAp (1.67) due to partial decomposition of HAp to TCP (*Eqs. 1 and 2*). Moreover, the HAp matrix found to contain measurable amount of Si which could be due to its substitution in HAp or TCP (*Eqs. 3 and 4*). Large variation in the composition was also observed from other deep etched regions (Points 7, 8 and 9 in **Figure 16**). For example, the phase labeled '7' in **Figure 16** found to have high concentration of Ca, Si and O, which indicates that this phase could be $CaSiO_3$ as observed in XRD (**Figure 15**).

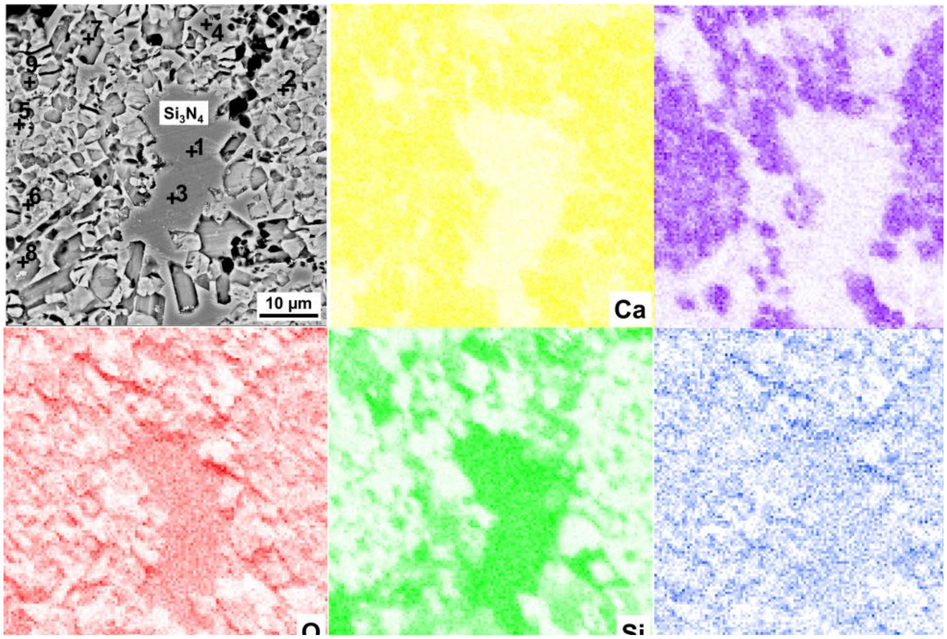

Figure 16. High-magnification SEM microstructure showing the distribution of different

Table 5. Average composition (at. %) of different phases, determined using EDX, observed in sintered HAp10SN samples. Points of compositional analysis are labeled in Figure 16.

	Si$_3$N$_4$	**HAp matrix**	**Deep etched regions**		
	Points: 1, 3, 4	**Points: 2, 5, 6**	**Point: 7**	**Point: 8**	**Point: 9**
Si	21.1 ± 1.1	2.3 ± 1.9	23	9.4	3.8
N	7.8 ± 0.3	8.9 ± 0.5	7.3	9	7.9
Ca	3.8 ± 0.1	13.3 ± 1.1	21.7	5.6	15.6
P	0.9 ± 0.2	11.5 ± 1.2	1.5	3.8	12.9
O	66.3 ± 1.2	63.9 ± 1.5	46.6	72.1	59.7

The above results indicate that present CF^3 processed HAp10SN samples containing ~ 15% total porosity with Si-substituted HAp or TCP and Si_3N_4 particles could show potentially superior biological performance than pure HAp samples. For example, Si-substituted calcium phosphates (HAp or TCP) can enhance bone healing [51, 52] through active release of Si ions (thus influencing cellular activities) and physico-chemical changes such as grain size, surface protein adhesion, surface topography changes, brought out by the presence of Si in the structure of HAp or TCP. Additional presence of Si_3N_4 in the present composites is expected to promote osteoblast activity [36] and inhibit bacterial growth [37, 38]. Further, any release of Si_3N_4 particles from the composite can dissolve in the physiological media and demonstrated to have improved body acceptance [53]. However, further studies are required to achieve microstructural uniformity along with evaluation of anticipated biological performance of these CF^3 processed HAp and HAp10SN ceramics.

3.4 Summary

Hydroxyapatite (HAp) and HAp with 10 wt.% Si_3N_4 (HAp10SN) samples were successfully fabricated using ceramic fused filament fabrication (CF^3). The viscosity of green filaments, with 63 wt.% ceramic powder, increased with addition of Si_3N_4 due to its finer size and irregular shape, which also resulted in relatively more binder removal during solvent debinding. CF^3 of these feedstocks produced defect free samples with relative density of ~ 85% after sintering at 1250 °C for 4 h. The microstructural refinement due to the presence of Si_3N_4 in the HAp matrix resulted in improvement in the hardness from 81 HV to 384 HV. The sintered HAp10SN samples also exhibited relatively smoother surface than pure HAp samples. The XRD analysis showed the presence of HAp and TCP with potential Si-substitution and discrete Si_3N_4 particles in HAp10SN samples. These compositional modifications with ~ 15% total porosity and high hardness of HAp-Si_3N_4 samples show their strong potential of superior biological performance than pure HAp and further detailed investigations are advocated to achieve microstructural uniformity and confirm the anticipated biological performance of these CF^3 processed HAp10SN ceramics for bone replacement applications.

CHAPTER 4

CONCLUSIONS

A Taguchi L9 based design of experiments (DOE) was successfully conducted with 75 wt. % HAp CF^3 printed parts to identify the extent by which the print process parameters affect the printed part properties. Additionally, A HAp ceramic and Hap10SN ceramic matrix composite with 75 wt.% solids loading filaments were CF^3 3D printed into test geometries, debound and sintered successfully to obtain defect free parts with comparable densities. Conclusions for these studies are summarized below:

- Regression analysis performed on printing process parameters indicates that the models generated had an excellent closeness of fit with R^2 ranging between 90-99 with relative density being an exception of 70% R^2.
- Extrusion multiplier found to be the most significant parameter in dictating the final part properties followed by print speed. The effect becomes more significant at lower infill percentages.
- It can be said that the geometrical part properties are determined by the combined effects of extrusion multiplier and print speed, this combined factor is equivalent to the volume of material extruded per unit area per unit time in a print. Over extrusion or under extrusion may result in deviation from expected specification.

- For our experiments, lower extrusion multiplier of around 0.8 a.u. coupled with low printing speeds of 10 to 15 mm/s resulted in best parts having closest observed properties to the input or expected properties.

- This work allows for identification of key parameters that influence the part quality in ceramic fused filament fabrication. Consequently, with proper analysis and information about the extent of influence, the parameters can be modified beforehand to achieve the desired part quality.
- Hydroxyapatite (HAp) and HAp with 10 wt.% Si_3N_4 (HAp10SN) samples were successfully fabricated using ceramic fused filament fabrication (CF^3).
- Addition of Si_3N_4 resulted in an increase in viscosity of green filaments. This increase in viscosity wasn't as large as to hinder the extrusion of filaments while printing. This can be attributed to the finer size and irregular shape of Si_3N_4 powder particles.
- Sintering for 4 hours at 1250 °C resulted in ~ 85% dense parts with no defects. The sintered HAp10SN samples exhibited relatively smoother surface than pure HAp samples
- The microstructural refinement due to the presence of Si_3N_4 in the HAp matrix resulted in improvement in the hardness from 81 HV to 384 HV
- The XRD analysis showed the presence of HAp and TCP with potential Si-substitution and discrete Si_3N_4 particles in HAp10SN samples. These compositional modifications with ~ 15% total porosity and high hardness of HAp-Si_3N_4 samples show their strong potential of superior biological performance than

pure HAp and further detailed investigations are advocated to achieve microstructural uniformity and confirm the anticipated biological performance of these CF^3 processed HAp10SN ceramics for bone replacement applications.

CHAPTER 5

FUTURE WORK

A major part of the study deals with fabrication of HAp structures for application in utilization in biomedical implants. However, the printed geometries included simple 3D shaped such as cuboids and cylinders. Experiments in future will be conducted to CF^3 3D print specific implants-based design geometries which would be debound and sintered to study the effect of geometries on the part properties and quality of sintered parts.

Additionally, experiments will be conducted to study the bioactivity of sintered HAp structures in in-vitro conditions. This can be done by monitoring the growth of a cell culture and the nature of interaction with 3D printed HAp structures.

Another study can be conducted to realize the superior biological performance of HAp+Si_3N_4 composites compared to pure HAp. This hypothesis can be tested by comparing the mechanical properties and bioactivity in in-vitro conditions for both.

Current study uses a 40 vol.% solids loading of Hap and HAp10SN composites. Furture studies can be performed by preparing feedstocks with higher solids loading of up to 55 vol.%. This can possibly result in higher sintered density and hence better mechanical properties.

The maximum amount of Si_3N_4 used for preparing HAp+ Si_3N_4 composites for this study was 10 wt%. Higher proportions can be tested for feasibility of 3D printing and further improvement of mechanical properties.

REFERENCES

1. Balla, V.K., et al., Biointegration of three-dimensional–printed biomaterials and biomedical devices, in Biointegration of Medical Implant Materials. 2020. p. 433-482.

2. El-Ghannam, A., Bone reconstruction: from bioceramics to tissue engineering. Expert Rev Med Devices, 2005. 2(1): p. 87-101.

3. Mucalo, M., Hydroxyapatite for Biomedical Applications. 2015.

4. Reger, N.C., et al., Structural and phase analysis of multi-ion doped hydroxyapatite for biomedical applications. Ceramics International, 2019. 45(1): p. 252-263.

5. Ashby, M.F., Materials Selection in Mechanical Design. 2016: Elsevier Science.

6. Kate, K.H., R.K. Enneti, and S.V. Atre, Influence of feedstock properties on the injection molding of aluminum nitride. The International Journal of Advanced Manufacturing Technology, 2016. 90(9-12): p. 2813-2826.

7. Kate, K.H., et al., Simulations and injection molding experiments for aluminum nitride feedstock. Ceramics International, 2016. 42(1): p. 194-203.

8. Dutta Roy, T., et al., Performance of hydroxyapatite bone repair scaffolds created via three-dimensional fabrication techniques. J Biomed Mater Res A, 2003. 67(4): p. 1228-37.

9. Galante, R., C.G. Figueiredo-Pina, and A.P. Serro, Additive manufacturing of ceramics for dental applications: A review. Dent Mater, 2019. 35(6): p. 825-846.

10. Chen, Z., et al., 3D printing of ceramics: A review. Journal of the European Ceramic Society, 2019. 39(4): p. 661-687.

11. Bose, S., et al., Additive manufacturing of biomaterials. Prog Mater Sci, 2018. 93: p. 45-111.

12. Esposito Corcione, C., et al., Highly loaded hydroxyapatite microsphere/ PLA porous scaffolds obtained by fused deposition modelling. Ceramics International, 2019. 45(2): p. 2803-2810.

13. Singh, P., et al., Printability studies of Ti-6Al-4 V by metal fused filament fabrication (MF3). International Journal of Refractory Metals and Hard Materials, 2020.

14. Singh, P., et al., Estimating Powder-Polymer Material Properties Used in Design for Metal Fused Filament Fabrication (DfMF3). Jom, 2019. 72: p. 485-495.

15. Dey, A. and N. Yodo, A Systematic Survey of FDM Process Parameter Optimization and Their Influence on Part Characteristics. Journal of Manufacturing and Materials Processing, 2019. 3(3).

16. Gurrala, P.K. and S.P. Regalla, DOE Based Parametric Study of Volumetric Change of FDM Parts. Procedia Materials Science, 2014. 6: p. 354-360.

17. Gurrala, P.K. and S.P. Regalla, Multi-objective optimisation of strength and volumetric shrinkage of FDM parts. Virtual and Physical Prototyping, 2014. 9(2): p. 127-138.

18. Montero, M., et al. Material Characterization of Fused Deposition Modeling (FDM) ABS by Designed Experiments. in Proceedings of Rapid Prototyping & Manufacturing Conference. 2001. Cincinnati, OH, USA: Society of Manufacturing Engineers. .

19. Zaman, U.K.u., et al., Impact of fused deposition modeling (FDM) process parameters on strength of built parts using Taguchi's design of experiments. The International Journal of Advanced Manufacturing Technology, 2018. 101(5-8): p. 1215-1226.

20. Sudan, K., Processing of Hydroxyapatite and its composites using Ceramic Fused Filament Fabrication (CF3). Under review, 2020.

21. Castro e Costa, E., J.P. Duarte, and P. Bártolo, A review of additive manufacturing for ceramic production. Rapid Prototyping Journal, 2017. 23(5): p. 954-963.

22. Wang, J.-C., H. Dommati, and S.-J. Hsieh, Review of additive manufacturing methods for high-performance ceramic materials. The International Journal of Advanced Manufacturing Technology, 2019. 103(5-8): p. 2627-2647.

23. Singh, P., et al., Estimating Powder-Polymer Material Properties Used in Design for Metal Fused Filament Fabrication (DfMF3). Jom, 2019.

24. Rane, K. and M. Strano, A comprehensive review of extrusion-based additive manufacturing processes for rapid production of metallic and ceramic parts. Advances in Manufacturing, 2019. 7(2): p. 155-173.

25. M, M., Hydroxyapatite for Biomedical Applications. 2015.

26. Reger, N.C., et al., In vitro cytotoxicity and ion release of multi-ion doped hydroxyapatite. International Journal of Applied Ceramic Technology, 2018. 16(2): p. 503-516.

27. Šupová, M., Substituted hydroxyapatites for biomedical applications: A review. Ceramics International, 2015. 41(8): p. 9203-9231.

28. de Lima, M.G., et al., Microstructural and Mechanical Properties of Al₂O₃/HAp Composites for Use as Bone Substitute Material. Materials Science Forum, 2018. 912: p. 153-158.

29. Bollino, F., E. Armenia, and E. Tranquillo, Zirconia/Hydroxyapatite Composites Synthesized Via Sol-Gel: Influence of Hydroxyapatite Content and Heating on Their Biological Properties. Materials (Basel), 2017. 10(7).

30. Schumacher, T.C., L. Treccani, and K. Rezwan, Effect of silica on porosity, strength, and toughness of pressureless sintered calcium phosphate-zirconia bioceramics. Biomed Mater, 2015. 10(4): p. 045020.

31. Zilm, M., S.D. Thomson, and M. Wei, A Comparative Study of the Sintering Behavior of Pure and Manganese-Substituted Hydroxyapatite. Materials (Basel), 2015. 8(9): p. 6419-6436.

32. Constanda, S., et al., Carbon Nanotubes-Hydroxyapatite Nanocomposites for an Improved Osteoblast Cell Response. Journal of Nanomaterials, 2016. 2016: p. 1-10.

33. Rahaman, M. and W. Xiao, Silicon nitride bioceramics in healthcare. International Journal of Applied Ceramic Technology, 2018. 15(4): p. 861-872.

34. Pezzotti, G., et al., Silicon Nitride: A Synthetic Mineral for Vertebrate Biology. Sci Rep, 2016. 6: p. 31717.

35. Das, M., K. Bhimani, and V.K. Balla, In vitro tribological and biocompatibility evaluation of sintered silicon nitride. Materials Letters, 2018. 212: p. 130-133.

36. Pezzotti, G., et al., Bioactive silicon nitride: A new therapeutic material for osteoarthropathy. Sci Rep, 2017. 7: p. 44848.

37. Gorth, D.J., et al., Decreased bacteria activity on Si(3)N(4) surfaces compared with PEEK or titanium. Int J Nanomedicine, 2012. 7: p. 4829-40.

38. Webster, T.J., et al., Anti-infective and osteointegration properties of silicon nitride, poly(ether ether ketone), and titanium implants. Acta Biomater, 2012. 8(12): p. 4447-54.

39. Bal, B.S. and M.N. Rahaman, Orthopedic applications of silicon nitride ceramics. Acta Biomater, 2012. 8(8): p. 2889-98.

40. Kate, K.H., et al., Feedstock properties and injection molding simulations of bimodal mixtures of nanoscale and microscale aluminum nitride. Ceramics International, 2013. 39(6): p. 6887-6897.

41. Tlegenov, Y., W.F. Lu, and G.S. Hong, A dynamic model for current-based nozzle condition monitoring in fused deposition modelling. Progress in Additive Manufacturing, 2019. 4(3): p. 211-223.

42. Anandan, D. and A.K. Jaiswal, Synthesis and characterization of human bone-like hydroxyapatite using Schiff's base. Ceramics International, 2018. 44(8): p. 9401-9407.

43. Kapat, K., et al., Influence of Porosity and Pore-Size Distribution in Ti6Al4 V Foam on Physicomechanical Properties, Osteogenesis, and Quantitative Validation of Bone Ingrowth by Micro-Computed Tomography. ACS Appl Mater Interfaces, 2017. 9(45): p. 39235-39248.

44. Feng, P., et al., A novel two-step sintering for nano-hydroxyapatite scaffolds for bone tissue engineering. Sci Rep, 2014. 4: p. 5599.

45. Plucknett, K., Sintering Behavior and Microstructure Development of Porous Silicon Nitride Ceramics Prepared in an Air Atmosphere Furnace. International Journal of Applied Ceramic Technology, 2009. 6(6): p. 702-716.

46. Li, X.W., H.Y. Yasuda, and Y. Umakoshi, Bioactive ceramic composites sintered from hydroxyapatite and silica at 1,200 degrees C: preparation, microstructures and in vitro bone-like layer growth. J Mater Sci Mater Med, 2006. 17(6): p. 573-81.

47. Langstaff, S., Resorbable bioceramics based on stabilized calcium phosphates. Part I: rational design, sample preparation and material characterization. Biomaterials, 1999. 20(18): p. 1727-1741.

48. Reid, J.W., et al., Phase formation and evolution in the silicon substituted tricalcium phosphate/apatite system. Biomaterials, 2005. 26(16): p. 2887-97.

49. Sayer, M., et al., Structure and composition of silicon-stabilized tricalcium phosphate. Biomaterials, 2003. 24(3): p. 369-382.

50. Pulkin, M., D. Koch, and G. Grathwohl, Silica Effect on Porous Calcium Phosphate Ceramics from the Freeze Gelation Route. International Journal of Applied Ceramic Technology, 2011. 8(6): p. 1414-1424.

51. Bartkowiak, A., et al., Biological effect of hydrothermally synthesized silica nanoparticles within crystalline hydroxyapatite coatings for titanium implants. Mater Sci Eng C Mater Biol Appl, 2018. 92: p. 88-95.

52. Bohner, M., Silicon-substituted calcium phosphates - a critical view. Biomaterials, 2009. 30(32): p. 6403-6.

53. Olofsson, J., et al., Evaluation of silicon nitride as a wear resistant and resorbable alternative for total hip joint replacement. Biomatter, 2012. 2(2): p. 94-102.

APPENDICES

APPENDIX A: CF^3 OF POLYMER DERIVED CERAMICS(PDCs)

- Alumina powder along with a preceramic polymer Z-6018 used as filler in polymer matrix to create ceramic composite filament.
- Z-6018 is a commercially available silicone resin from Dow Corning. Chemically, it is a mixture of phenyl, propyl silsesquioxanes (> 60%) and a hydroxyl terminated linear siloxane

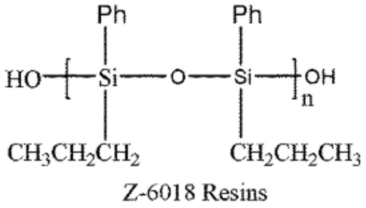

Figure A1. Chemical structure of Z-6018 resin

- Z-6018 has a Ceramic yield of about 73% (from TGA)
- Expected compounds on pyrolysis of Z-6018:
    - SiO_2
    - SiC
    - $SiOC$

Table A1. Feedstock Composition for PDC composite

Component	**Weight fraction (in %)**
Alumina	60
Z-6018	20
Polymer blend	40

Table A2. Feedstock Preparation and Filament extrusion parameters

Batch no.	Mixing time (in mins)	Extrusion temperature (in ^{0}C)	Extrusion Speed (in mm/s)
1	40	85	0.1
2	80	100	0.1
3	120	112	0.1

Table A3. Print parameters for 3D printing of PDC composite parts

Extrusion Temperature	210 ^{0}C
Bed Temperature	50 ^{0}C
Print speed	10 mm/s
layer thickness	0.25 mm
Nozzle size	0.5 mm

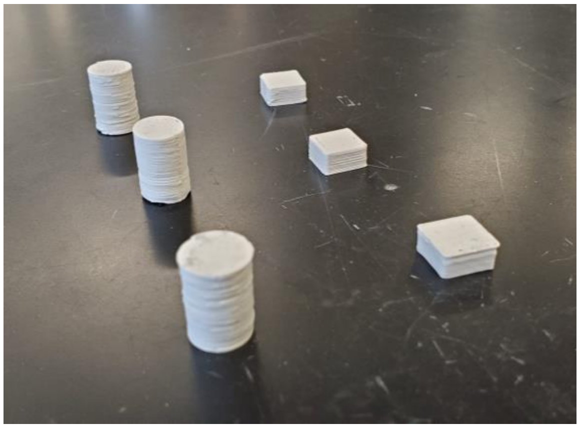

Figure A2. Green parts with different geometries printed using PDC composite filament.

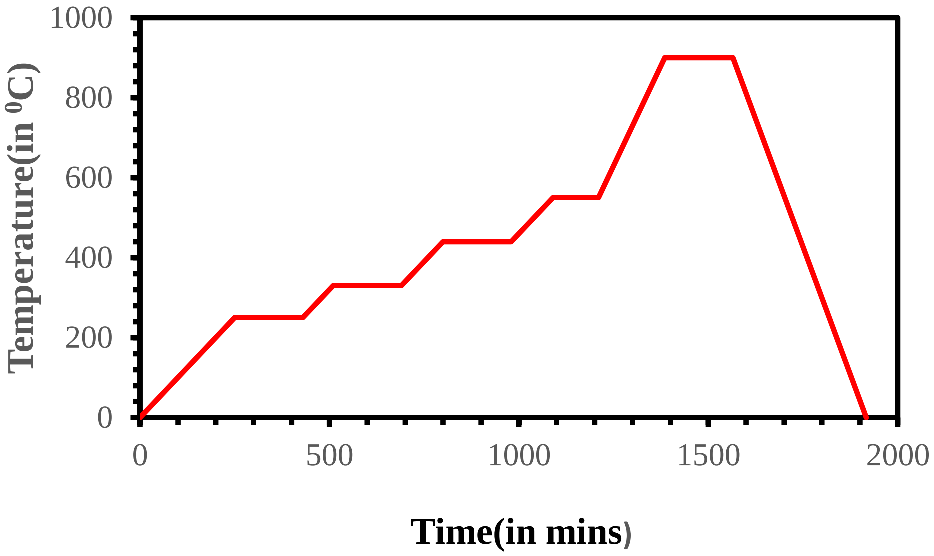

Figure A3. Thermal debinding cycle for green PDC composite parts.

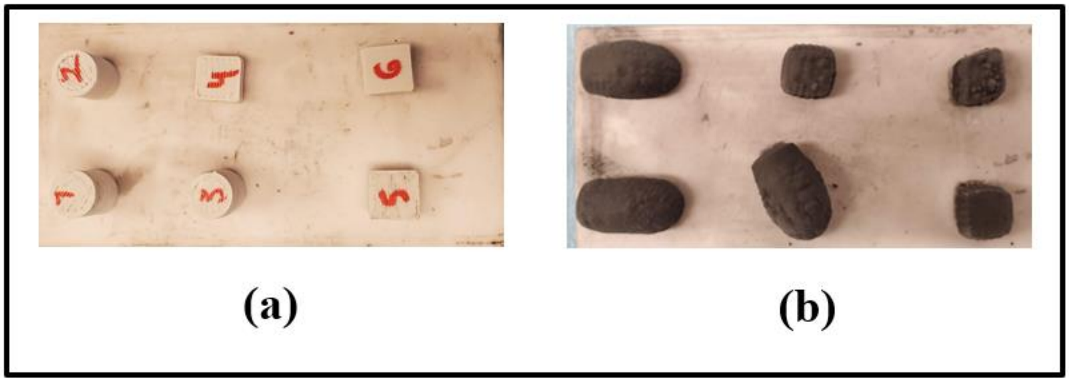

Figure A4. (a) PDC composite parts before debinding. (b) Composite parts after thermal debinding up to 850 ^{0}C.

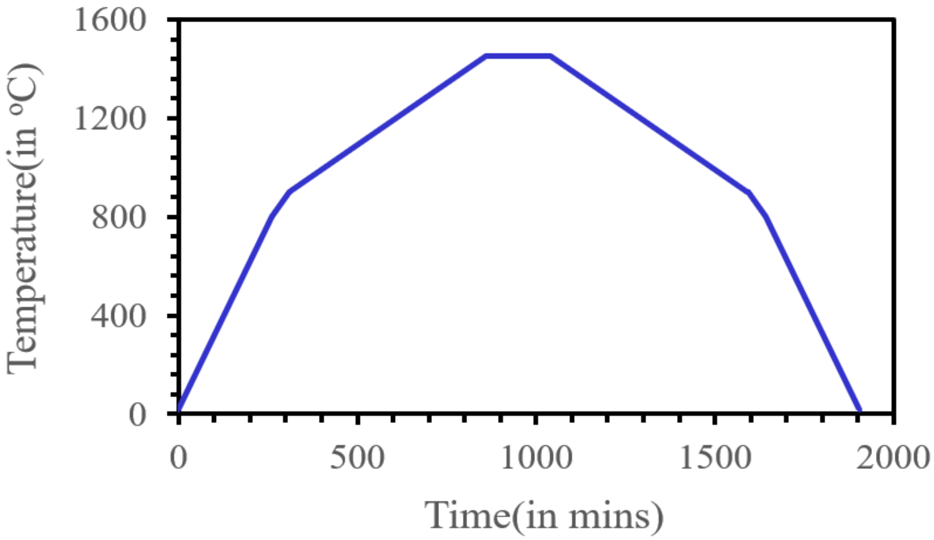

Figure A5. Sintering cycle for thermally debound PDC composite parts.

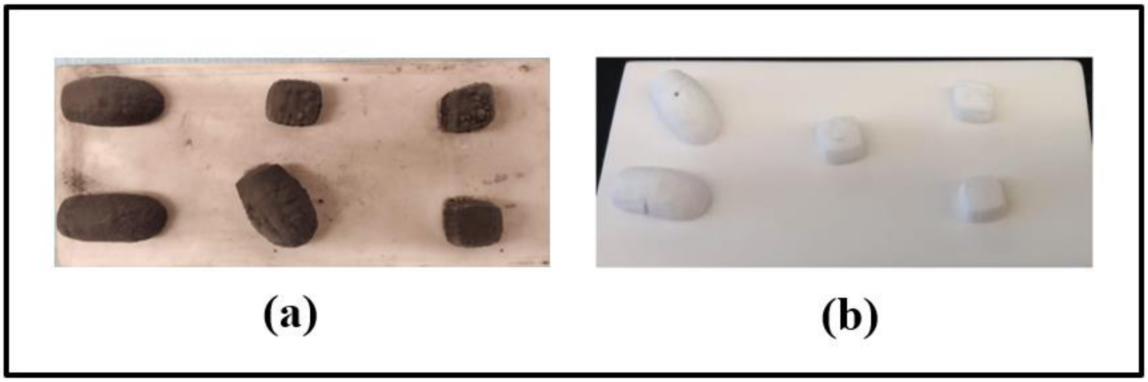

Figure A6. (a) Thermally debound parts. (b) PDC composite parts after sintering up to 1450 °C.

APPENDIX B: CONTINUOUS FIBER 3D PRINTING AND NOZZLE DESIGN

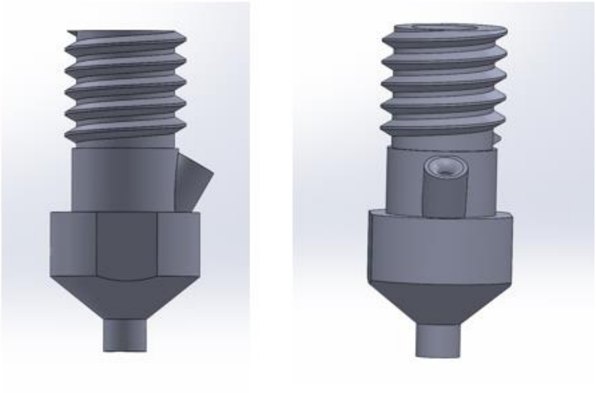

Figure B3. CAD model of nozzle design for co-extrusion of continuous fiber and polymer filament.

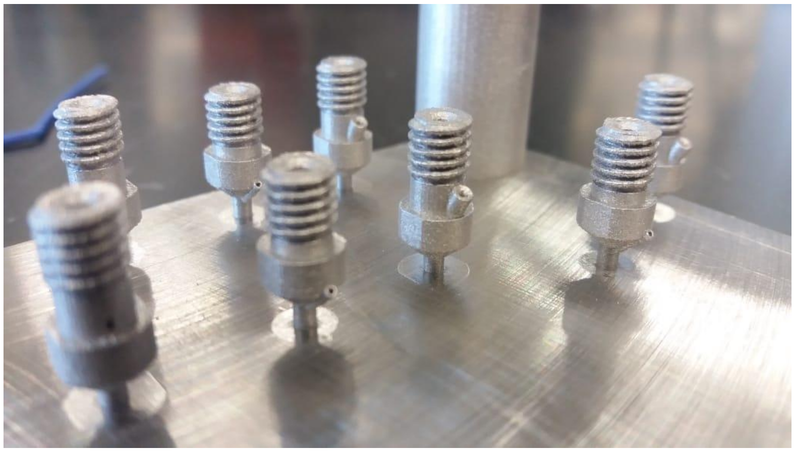

Figure B2. 1 mm dia nozzles printed using L-PBF.

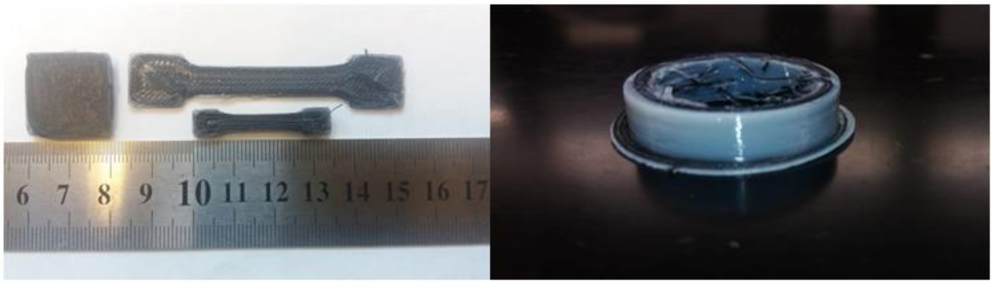

Figure B3. Composite parts printed using co-extrusion of textile fibers and PLA polymer.

CURRICULUM VITA

NAME: Kavish Sudan
ADDRESS: 2330 Crittenden Drive, KY – 40217
DOB: Jammu, India – March 24, 1995
Education
and training: B.Eng., Mechanical Engineering
University of Jammu
2013-17
M.S., Mechanical Engineering
University of Louisville, Kentucky
2019-21
Awards: MPIF Student Grant Recipient
2019
National Science Foundation Student Grant Recipient
2020
Professional
societies: American Powder Metallurgy Institute
2019-21

Publications:

First Author:

- Processing of Hydroxyapatite and its composites using Ceramic Fused Filament Fabrication (CF^3). DOI: 10.1016/j.ceramint.2020.06.168

Second Author:

- First report on fabrication and characterization of soybean hull fiber: polymer composite filaments for fused filament fabrication. DOI: 10.1007/s40964-020-00138-2
- Digital Design and Manufacturing with Thermomechanical Process Simulation for Fused Filament Fabrication 3D Printing. DOI: 10.12783/asc35/34848